



Comparison of empirical interatomic potentials for iron applied to radiation damage studies

L. Malerba^{a,*}, M.C. Marinica^b, N. Anento^c, C. Björkas^d, H. Nguyen^e, C. Domain^f, F. Djurabekova^d, P. Olsson^f, K. Nordlund^d, A. Serra^c, D. Terentyev^a, F. Willaime^b, C.S. Becquart^e

^aStructural Materials Group, Institute of Nuclear Materials Science, SCK-CEN, Boeretang 200, B-2400 Mol, Belgium

^bCEA, DEN, Service de Recherches de Métallurgie Physique, F-91191 Gif-sur-Yvette, France

^cDepartment Matemàtica Aplicada III, E.T.S. Enginyeria de Camins, Universitat Politècnica de Catalunya, Jordi Girona 1-3, 08034 Barcelona, Spain

^dDepartment of Physics, University of Helsinki, P.O. Box 43, FI-00014, Finland

^eUnité Matériaux et Techniques (UMET), UMR 8207, Université Lille-1, F-59655 Villeneuve d'Ascq Cédex, France

^fDept. MMC, EDF-R&D, Site des Renardières, F-77218 Moret-sur-Loing, France

A B S T R A C T

The performance of four recent semi-empirical interatomic potentials for iron, developed or used within the FP6 Perfect Project, is evaluated by comparing them between themselves and with available experimental or, more often, density functional theory data. The quantities chosen for the comparison are of specific interest for radiation damage studies, i.e. they concern mainly properties of point-defects and their clusters, as well as dislocations. For completeness, an earlier, widely used (also within the Project) iron potential is included in the comparison exercise as well. This exercise allows conclusions to be drawn about the reliability of the available potentials, while providing a snapshot of the state-of-the-art concerning fundamental properties of iron, thereby being also useful as a kind of handbook and as a framework for the validation of future semi-empirical interatomic potentials for iron. It is found that Mendelev-type potentials are currently the best choice in order to “extend density functional theory” to larger scales and this justifies their widespread use, also for the development of iron alloy potentials. However, a fully reliable description of self-interstitial atom clusters and dislocations with interatomic potentials remains largely an elusive objective, that calls for further effort within the concerned scientific community.

© 2010 Elsevier B.V. All rights reserved.

1. Introduction

A little before the start of the FP6 Perfect Project (henceforth simply the Project), a set of new semi-empirical interatomic potentials for body-centred-cubic iron (bcc-Fe) was published by Mendelev et al. [1]. Despite using a formalism that was far from new, i.e. the so-called embedded atom method [2], this set of potentials turned out to represent a significant advance, compared to the past. On the one hand, the fitting procedure was extremely careful and made use of a large set of fitting and validation data, including properties of the liquid phase and the melting point. On the other hand, point-defect energies calculated little before by means of density functional theory (DFT) techniques, especially the then-surprising energy difference between the dumbbell and crowdion configurations of the self-interstitial atom (SIA) in body-centred-cubic iron (bcc-Fe) [3], were used as a reference for the development of the potential. In particular, the potential “number 2” in [1] turned out to be especially accurate to describe a large

number of properties involving defects in bulk bcc-Fe, from small SIA clusters [4] to dislocations [5], when compared to DFT results and also experiments. This potential will be hereafter denoted as M03. At the beginning of the Project, a slight modification of M03 was proposed as part of a potential for the FeP binary alloy [6] (henceforth denoted as A04). Either of these two potentials, M03 and A04, has been next extensively used, within and without the Project, both for studies of defect properties in pure Fe, often in comparison with other potentials or DFT results [4–15], and as a basis for the development of alloy potentials [4,16–21].

Within the Project, two more potentials for bcc-Fe have been developed: the so-called ‘magnetic’ potential proposed in [22] and the set of Mendelev-type potentials still being worked on at CEA-Saclay. The former is based on a combination of the Stoner and the Ginzburg–Landau models and introduces, via a specific embedding functional form, an explicit magnetic contribution to the energy of interaction between atoms in α -Fe. The version herein used corresponds to case study II in [22] and is denoted as D05. The latter uses exactly the same formalism as for M03 and A04, but aims at better fitting a number of properties of importance for Fe that the original M03 and A04 are found not to reproduce satisfactorily. The version

* Corresponding author. Tel.: +32 14 333090; fax: +32 14 321216.
E-mail address: lmalerba@sckcen.be (L. Malerba).

Table 1
Basic properties of Fe as predicted by the different potentials and compared with either experimental or *ab initio* (in italics) data. Legend: a_0 , lattice parameter (RT room temperature); E_{coh} , cohesive energy (at 0 K and equilibrium lattice parameter); $\Delta E_{fcc-bcc}$, cohesive energy difference between bcc and fcc structures (in the case of the fcc phase: FM, ferromagnetic; NM, non-magnetic); C_{ij} , elastic constants; γ_{ijk} , surface energy for (*ijk*) surface; T_m , melting temperature; N/A, not available.

Description	A97	M03	A04	D05	M07	Exp. and/or <i>ab initio</i>
a_0 (bcc) (Å) ^A	2.866 ^{a,b}	2.855 ^{a,b}	2.855 ^c	2.866 ^b	2.856	2.860 (0 K) ^d 2.870 (RT) ^e
a_0 (fcc) (Å)	3.680 ^{a,b}	3.658 ^b	3.658	3.608 ^b	3.668	3.658 ^a
E_{coh} (bcc) (eV/atom)	4.316 ^{a,b}	4.122 ^a , 4.127 ^b	4.013 ^a	4.316 ^{b,f}	4.122	4.280 ^e
$\Delta E_{fcc-bcc}$ (eV/atom)	0.054 ^a	0.121 ^b	0.121 ^g	0.086 ^b , 0.1355 ^f (FM); 0.2216 ^f (NM)	0.122	0.122 ^a , 0.035 ^b , 0.08 ^h , 0.050 ⁱ
C_{11} (GPa)	243.4 ^a	243.4 ^a	243.3	243.4	243.3	243 ^k , 233 ^l , 237 ^m , 226 ⁿ
C_{12} (GPa)	145 ^a	145 ^a	145	145, 138 ^b	144	138 ^k , 135 ^l , 141 ^m , 140 ⁿ
C_{44} (GPa)	116 ^a	116 ^a	116	121	121	122 ^k , 118 ^l , 116 ^{m,n}
γ_{100} (mJ m ⁻²)	1810 ^a	1762 ^a	1752	1799 ^p	2012	2179 ^a
γ_{110} (mJ m ⁻²)	1580	1651	1617	1624	1869	N/A
γ_{111} (mJ m ⁻²)	1997	1998	1964	1998	2315	N/A
T_m (K)	2358 ^a (coexistence temperature), 2340 ± 20 ^b (moving interface), 2396 ^q (thermodynamic integration)	1772 ^a (coexistence temperature), 1760 ± 20 ^b (moving interface)	1750 ± 25 ^r (moving interface)	2160 ± 20 ^b , 2175 ± 25 ^r (moving interface)	2250 ± 50 (moving interface)	1811 ^e

^A See Fig. 1 for thermal expansion.

^a Ref. [1].

^b Ref. [37].

^c Ref. [6].

^d Ref. [38].

^e Ref. [39].

^f Ref. [22].

^g Ref. [7].

^h Ref. [40].

ⁱ Ref. [41].

^j Ref. [42] (high temperature value).

^k Ref. [43].

^l Ref. [44].

^m Ref. [45].

ⁿ Ref. [46].

^p Ref. [47].

^q Ref. [48].

^r Ref. [10].

used here, denoted as M07, is briefly described in terms of parameters in Appendix A; full details about this set of potentials will be published elsewhere. Both D05 and M07 were produced having as reference the latest data concerning, in particular, the description of SIAs in bcc-Fe, from DFT calculations [3,4,23].

In the present work, a number of results obtained with these four potentials (M03, A04, D05 and M07) are compared between

themselves and with available experimental or, more often, DFT data. The quantities chosen for the comparison are of specific interest for radiation damage studies, i.e. they concern mainly properties of point-defects and their clusters, as well as dislocations. In most cases they are the result of static calculations, but a few results from dynamic studies (effective migration energies, displacement cascades, ...) are also presented. For completeness,

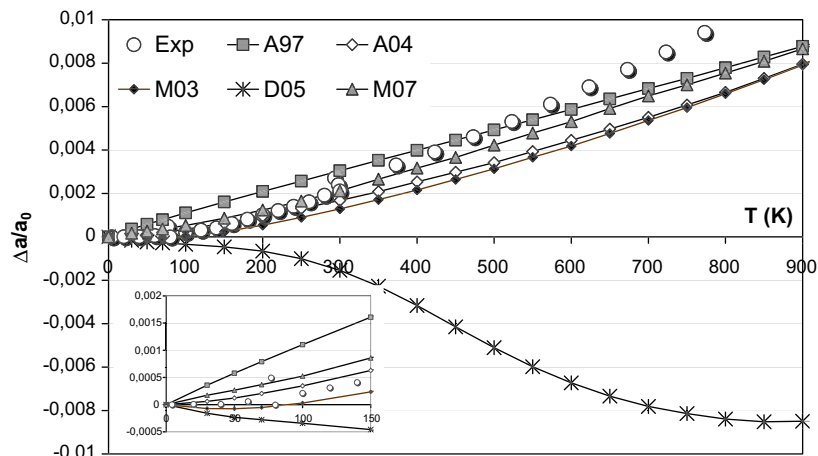


Fig. 1. Thermal expansion according to the different potentials. The inset blows up the low temperature behaviour. Note the odd thermal “contraction” predicted by D05 at all temperatures. The zero point motion is not taken into account in the calculation.

the bcc-Fe potential developed in [24], here denoted as A97, is also included in the comparison exercise. A97 is indeed a good example of an early many-body potential, i.e. fitted without allowing for the information that came from DFT since the year 2000. A97 has been widely used (also within the Project) for a variety of studies concerning radiation defect production, stability, mobility and interaction in bcc-Fe and FeCu alloys, especially on loops and dislocations [25–36]. It is therefore important to verify how the new potentials perform as compared to it.

This comparison exercise allows conclusions to be drawn about the reliability of the available potentials, by providing a snapshot of the state-of-the-art concerning fundamental properties of Fe that, in many cases, are not accessible to experiments. As such, this

exercise is also useful as a kind of handbook (many values will be of use for example for kinetic Monte Carlo simulations or rate theory models) and as a framework for the validation of future semi-empirical interatomic potentials or, in general, cohesive models for bcc-Fe.

Recently, a bond-order-type potential for Fe, also fitted to the DFT description of the relative stability of SIA, has been proposed [37]. The attractive feature of such a potential is its ability to describe the α - γ transition of Fe. Nonetheless, since this potential was neither produced, nor used within the Project, it is not included in the present comparison exercise. In the article where the potential is proposed there is, however, a quite extensive comparison with some of the potentials compared here. Concerning

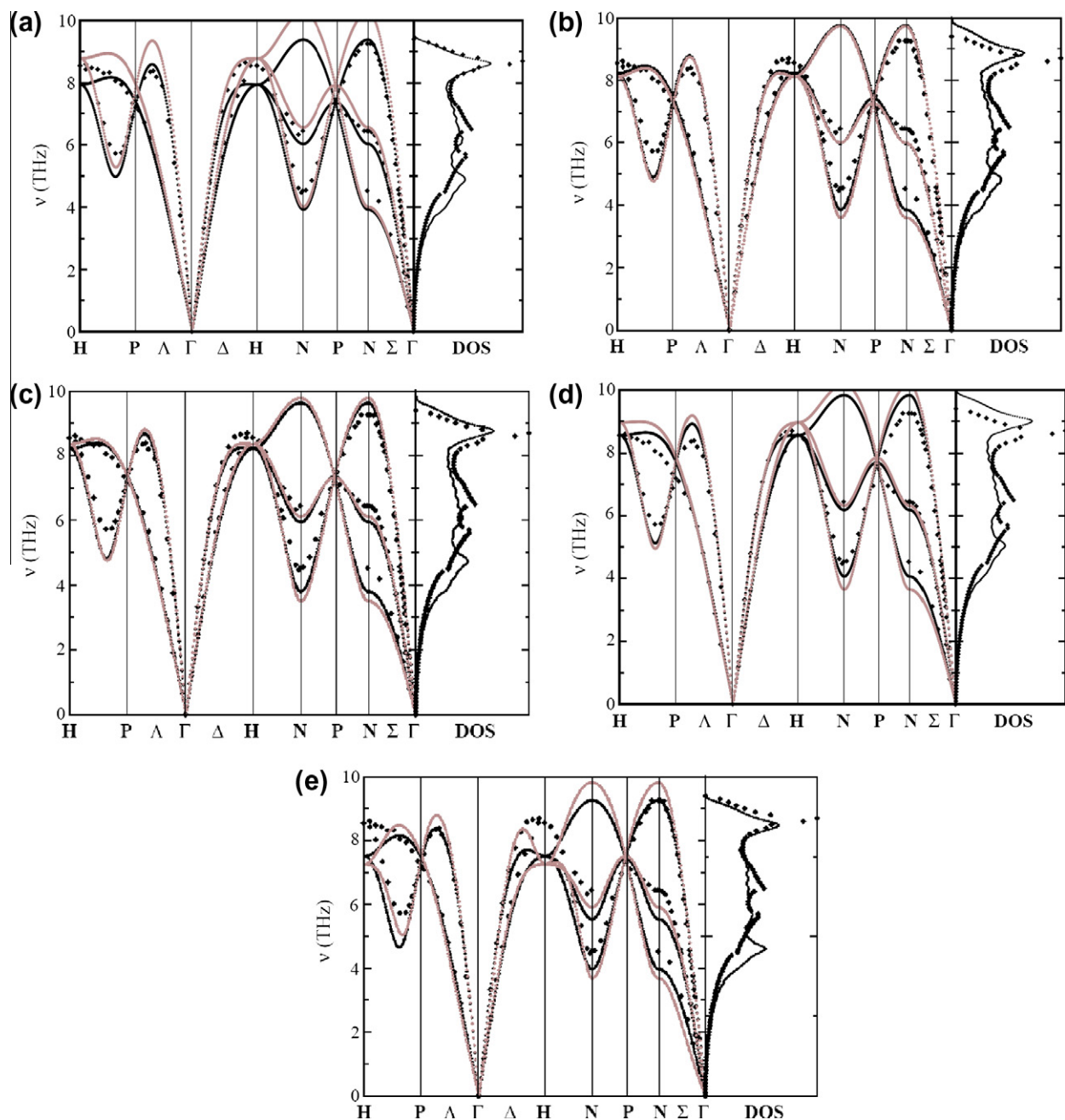


Fig. 2. Bulk phonon properties in iron. The experimental results at ambient pressure (diamond symbols, [44]) are compared with calculations performed using the different potentials at 0 pressure (full black line) and under pressure at 10 GPa (full color line). From (a) to (e) the presented results correspond to, respectively: A97, M03, A04, D05 and M07. The phonon dispersion curves are represented in the high symmetry directions. The phonon densities of states are calculated using 1623 special \mathbf{q} points (black solid line). For more details on the calculation, see [11]. (For interpretation of the references to color in this figure legend, the reader is referred to the web version of this article.)

displacement cascades, a comparison has been made in [10]. These results will be taken into account for the discussion.

In Section 2 we report the results of calculating basic properties such as elastic constants, lattice expansion and melting point. In Section 3 the fundamental properties of point-defects and small clusters thereof (mainly characteristic energies) are addressed. In Section 4 selected properties of dislocations and dislocation loops are explored. In Section 5 results concerning damage production in displacement cascades are given. In Section 6 a discussion and a few concluding remarks are provided.

For the details of the calculations in most cases the reader is necessarily referred to previous publications. Whenever the value has been taken from a published work, the reference is given. Almost all of such values have been, however, also re-calculated and verified. In some cases more than one value is reported, corresponding to slightly different calculation methods (different codes, different algorithms, ...). By reporting all values we provide an idea of the uncertainty related to these calculations, generally not larger than 0.1 eV for characteristic energies (the largest part of the reported database).

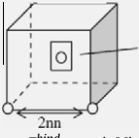
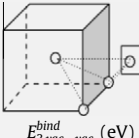
2. Basic properties

Table 1 shows a summary of basic properties of Fe, unrelated to radiation damage, as calculated with the different potentials and compared with experimental and DFT indications. Except for the melting point, all are the results of static calculations performed in standard way, i.e. by minimising the energy of the system in

the situation of interest or, in the case of elastic and lattice properties, by tracing the energy and force variation when applying appropriate lattice deformation. Zero temperature and pressure were assumed. Figs. 1 and 2 provide information about lattice expansion and phonon properties, respectively. The lattice expansion was calculated by performing constant pressure molecular dynamics simulations, while the procedure for obtaining the phonon dispersion curves is detailed in [11]. The reported melting points come from different estimations. The thermodynamic integration result for A97 comes from the construction of the whole phase diagram using the methodology described in [48]. The coexistence temperature method searches iteratively the temperature corresponding to zero values of the stresses in the bulk crystal and liquid phase and is briefly described in [1], where references are also given. The moving interface method is rougher, but based on the same idea as the coexistence temperature method (see e.g. [49]): solid and liquid phases are put in contact and the melting point is contained in the interval between the highest studied temperature at which the interface moves towards the liquid, thereby increasing the fraction of solid, and the lowest studied temperature at which the opposite occurs.

The cohesive energies and equilibrium lattice parameters are different depending on the potential. They are both, however, only reference values. These differences between potentials and with respect to the experimental value do not represent, therefore, a major shortcoming for the comparison, so long as the comparison is made between *differences with respect to the reference*, as is generally done. Concerning the energy difference between fcc and bcc

Table 2
Properties of vacancy-type defects in Fe (formation and binding energies mainly), as predicted by the different potentials in static calculations and compared with either experimental or, more often, *ab initio* (in italics) data. Legend: E stands for energy (V for volume, in units of atomic volumes, $\Omega_0 = a_0^3/2$); superscripts *for* and *bind* stand for *formation* and *binding*, respectively; the subscripts X_{vac} denote X vacancies in the considered cluster; X_{nn} stands for X th nearest neighbour. In the case of tri- and tetra-vacancy, the removed vacancy is indicated by a square around it in the inserted figure. For the difference between SIESTA and VASP-USPP/PAW (data obtained with the latter appear in bold), see Section 3.1.

Description	A97	M03	A04	D05	M07	Exp. and/or <i>ab initio</i>
E_{1vac}^{for} (eV)	1.70 ^{a,b}	1.71 ^b , 1.73 ^c	1.71 ^d , 1.74	1.86 ^b , 1.98	2.10	1.53 ^e , $\approx 2^f$, 1.95 ^g , 2.07 ^h , 2.02–2.15 ⁱ (depending on used DFT method)
V_{1vac}^{for} (Ω_0)	0.82 ^{a,b}	0.77 ^b	0.77 ^d	0.59 ^b , 0.83	0.90	0.95 ^j
E_{2vac}^{bind} (eV) 1 ⁿⁿ	0.14 ^d , 0.15	0.12, 0.13	0.13, 0.14 ^d	0.25	0.13, 0.14	0.14 ^k , 0.15 ^g , 0.14/ 0.16^d
E_{2vac}^{bind} (eV) 2 ⁿⁿ	0.18, 0.19 ^a	0.23, 0.24	0.23, 0.24 ^d	0.25, 0.26	0.32, 0.33	0.28 ^k , 0.29 ^g , 0.28/ 0.23^d , 0.30 ^m
E_{2vac}^{bind} (eV) 3 ⁿⁿ	–0.06	–0.02	–0.02	–0.03	–0.03	–0.02/– 0.015^d
E_{2vac}^{bind} (eV) 4 ⁿⁿ	0.04	0.03	0.03	0.04	0.04	0.09/ 0.05^d
E_{2vac}^{bind} (eV) 5 ⁿⁿ	–0.02	–0.02	–0.02	–0.01	–0.02	0.06/ 0.06^d
E_{3vac}^{bind} (eV)	0.34	0.28, 0.30	0.30	0.52	0.33	0.36 ^{g,k} , 0.37 ^m
 $E_{2vac-vac}^{bind}$ (eV)	0.62, 0.63	0.55, 0.57	0.58	0.82	0.75	0.70 ^{g,k} , 0.62 ^m
 $E_{3vac-vac}^{bind}$ (eV)						

^a Ref. [24].

^b Ref. [37] (the origin of the relatively large discrepancy with presently calculated values is unknown).

^c Ref. [1].

^d Ref. [6].

^e Ref. [58].

^f Ref. [59].

^g Ref. [3].

^h Ref. [23].

ⁱ Ref. [60].

^j Ref. [61].

^k Ref. [62].

^l This work, DFT–VASP–USPP/PAW (see [60] for calculation details).

^m Ref. [63].

structures, seen the scatter in DFT and experimental values, all potentials can be considered reasonable. However, this single value is hardly of any significance, as the whole equation of state for the two phases should be sampled in order to draw conclusions about the capability of the potential to describe them. In fact, none of the considered potentials is able to reproduce spontaneously the bcc-to-fcc transformation with rising temperature. As mentioned above, it is only very recently that a bond-order potential for Fe capable of doing so has been published [37]. The elastic constants are well reproduced by all potentials; they are, however, standard fitting parameters, so any defensible potential is expected to reproduce them. It is difficult to make conclusions concerning surface energies, having only one reference value available; it stands out, however, that all potentials provide similar numbers, except M07, which invariably gives higher values, closer to the only available experimental indication. The melting point is reasonably well predicted only by M03 and A04. The thermal expansion is acceptably reproduced by all potentials, except D05, which predicts thermal contraction instead (also M03 provides negative values at very low temperature, see inset in Fig. 1). The phonon properties at ambient pressure are reasonably well predicted by all potentials. However, the stiffening of phonon modes under pressure is underestimated, when compared to data in [45], by M03 – which predicts a softening – and by A04; this probably explains also why the thermal expansion tends to be somewhat underestimated by these potentials.

3. Fundamental properties of point-defects and their clusters

3.1. Calculation methods

Almost all values reported in this section are the result of static calculations. The largest amount of them are characteristic ener-

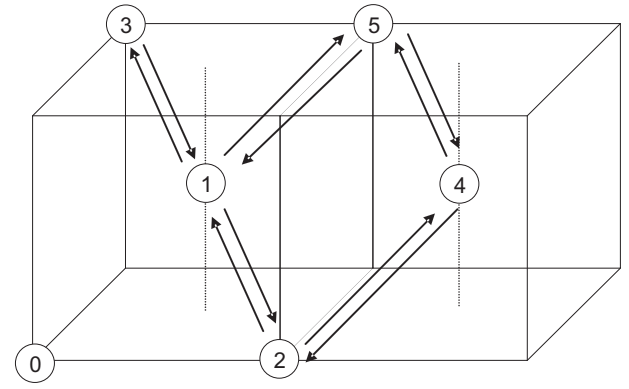


Fig. 3. Pictorial representation of the different possible di-vacancy configurations in a bcc structure and jumps of the second vacancy in the cluster (not all possible jumps are shown). Zero represents the position of the first vacancy; the other numbers correspond to the nearest neighbour shell at which the second vacancy is found with respect to the first one. In the case of Fe the ground state corresponds to two vacancies at 2nd nearest neighbour distance.

gies, i.e. formation, binding and migration energies. These are all equilibrium energy differences calculated with respect to a reference state, so discrepancies in the cohesive energy and equilibrium lattice parameters predicted by the different potentials do not question the validity of the comparison.

The formation energy is defined as the energy difference between the system with and without defect, at constant number of atoms. The binding energy is the difference between the formation energy of the system when the two involved defects are far apart and close to each other, according to the specified configuration: positive binding energies denote, therefore, attraction (the

Table 3

Properties of vacancy-type defects in Fe (migration energies), as predicted by the different potentials in calculations performed in different ways, compared with either experimental or, more often, *ab initio* (in italics) data. Legend: E_{1vac}^{mig} stands for migration energy, the subscript *2nd vac in di-vac* denotes the second vacancy in a di-vacancy (the transitions to which the energy barriers refer are pictorially indicated in Fig. 3); Xnn stands for Xth nearest neighbour; AKMC is Atomistic kinetic Monte Carlo (see [64] for methodology); NEB is nudged elastic bands (see [65,66] for methodology). Mechanisms (4nn and 1nn) are two different jump sequences for the di-vacancy (stable configuration is 2nn) to migrate: one vacancy jumps to 4nn and the other follows, or one vacancy jumps to 1nn and the other jumps away to 2nn (see [67] for further discussion). Effective values are those characteristic of the whole cluster. For the difference between USPP and PAW (data obtained with the latter are in bold), see Section 3.1.

Description	A97	M03	A04	D05	M07	Exp. and/or <i>ab initio</i>
Static E_{1vac}^{mig} (eV) [in parenthesis, height of double saddle point – see Fig. 4 for energy profiles] ^A	0.78 ^a , 0.79 ^b	0.63(0.11) ^c , 0.65(0.12)	0.63 ^{a,b} , 0.64(0.12)	0.84 ^b , 0.85(0.06)	0.68	0.55 ^{d,e} , 0.57 ± 0.14 ^f , 0.64 ^g , 0.67 ^h
E_{2vac}^{mig} in di-vac (eV) [1nn → 2nn/2nn → 1nn (w_3/w_4)]	0.85/0.89, 0.86/0.90	0.60/0.69, 0.61/0.71	0.62/0.70	0.89/0.89	0.61/0.81, 0.62/0.82	0.61/0.72, 0.58/0.67 ⁱ
E_{2ndvac}^{mig} in di-vac (eV) [1nn → 3nn/3nn → 1nn (w'_3/w'_4)]	1.04/0.83	0.83/0.67, 0.84/0.69	0.85/0.67, 0.86/0.69	1.10/0.82	0.94/0.77	0.87/0.71, 0.82/0.64 ⁱ
E_{2ndvac}^{mig} in di-vac (eV) [1nn → 5nn/5nn → 1nn (w''_3/w''_4)]	0.83/0.66, 0.83/0.67	0.72/0.56, 0.73/0.57	0.74/0.56, 0.74/0.58	0.89/0.62, 0.89/0.63	0.78/0.62, 0.77/0.61	0.70/0.62, 0.68/0.58 ⁱ
E_{2ndvac}^{mig} in di-vac (eV) [2nn → 4nn/4nn → 2nn (w_5/w_6)]	0.75/0.60, 0.76/0.62	0.63/0.42, 0.63/0.43	0.64/0.43, 0.64/0.44	0.83/0.61	0.70/0.41, 0.72/0.43	0.67/0.47, 0.68/0.50 ⁱ
E_{2vac}^{mig} (eV) [effective value]	0.75 (AKMC) ^b , 0.74 (NEB, 4nn mech.), 0.89 (NEB, 1nn mech.)	0.62 (AKMC) ^b , 0.62 (NEB, 4nn mech.)	0.63 (AKMC) ^b , 0.63 (NEB, 4nn mech.), 0.71 (NEB, 1nn mech.)	0.83 (AKMC) ^b , 0.83 (NEB, 4nn mech.), 0.89 (NEB, 1nn mech.)	0.70 (NEB, 4nn mech.), 0.77 (NEB, 1nn mech.)	0.62 (static, 1nn mechanism) ^h , 0.68–0.66 (AKMC based on <i>ab initio</i> barriers: USPP–PAW)
E_{3vac}^{mig} (eV) [effective value]	0.83 (static, NEB)	N/A	0.46 (AKMC) ^b , 0.45 (NEB)	0.80 (NEB)	0.53 (NEB) ^c	0.35 (static) ^h

^A Further data from Ref. [37] exist but are not included because they are suspiciously low, suggesting a systematic mistake in them.

^a Ref. [24].

^b Ref. [63].

^c Ref. [1].

^d Ref. [68].

^e Ref. [69].

^f Ref. [70].

^g Ref. [62].

^h Ref. [63].

ⁱ This work, DFT–VASP–USPP/PAW (see [60] for calculation details).

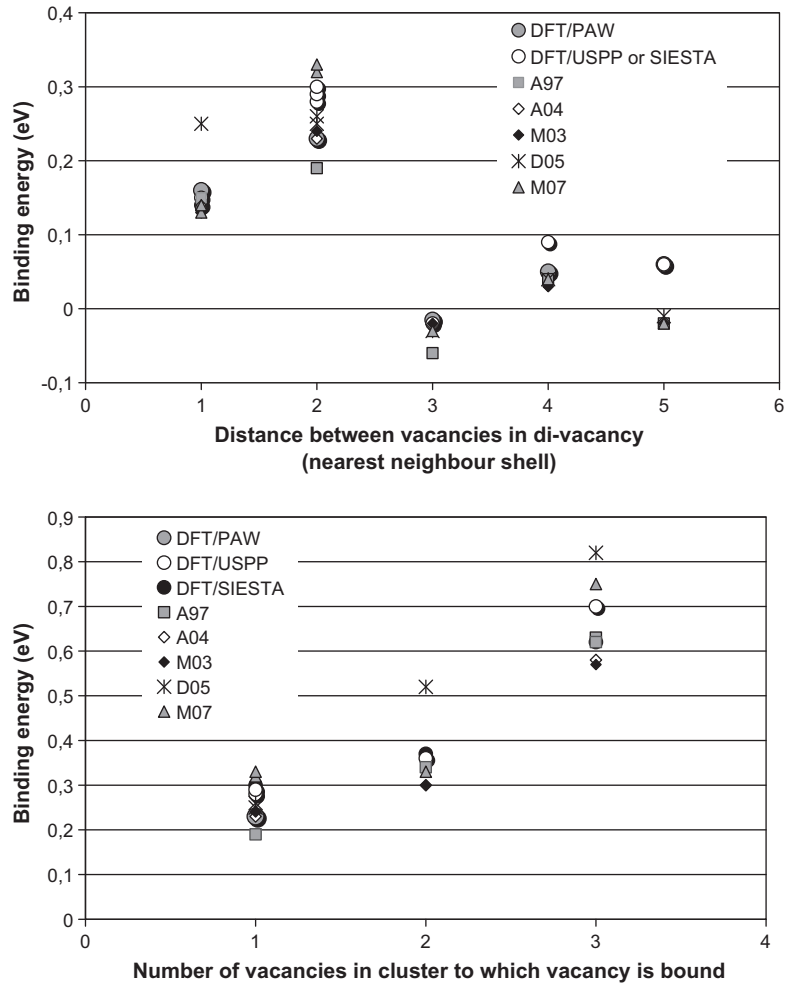


Fig. 4. Summary of data on vacancy-type defect binding energies. Upper panel: di-vacancy binding energy versus distance between the two vacancies (in terms of nearest neighbour shells, see Fig. 3); lower panel: binding energy of a vacancy to a cluster of specified size (most strongly bound cluster in all cases). For the differences between DFT methods, see Section 3.1.

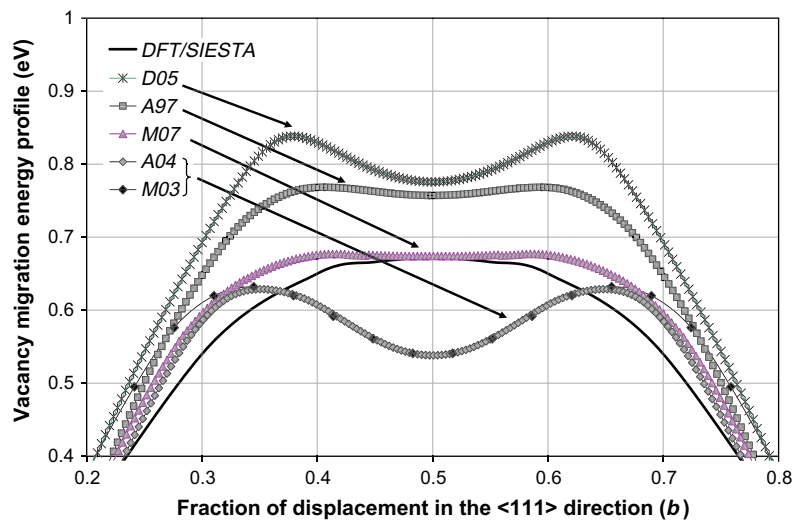


Fig. 5. Single-vacancy migration profile in the vicinity of the saddle point as calculated with the different potentials. This zoom on the saddle point description shows clearly that some potentials predict a double hump, with a local minimum in the intermediate position, that does not appear in DFT calculations (with SIESTA, see Section 3.1). The depth of the saddle point well is provided in each case in Table 3, first row.

energy *decreases* by putting the defects together), while negative binding energies denote repulsion (the energy *increases* by putting

the defects together). Finally, the migration energy is, by definition, the difference between the energy of the system at the saddle point

of the transition corresponding to a specific diffusion jump of the defect, and the energy of the system before the transition.

In static calculations the system is typically set in the configuration of interest and the energy is minimised by letting the atoms reach their equilibrium positions in such a configuration at zero temperature. Different methods can be used for this minimisation, e.g. quasi-dynamic quench [46,47] or conjugate gradient procedures [48]. In addition, the calculation can be performed at constant volume or constant pressure. Finally, the number of atoms included in the simulation box may differ. Altogether, this causes slight differences in the obtained values to be possible, even using the same potential and for the same defect, depending on the method. These differences are, however, generally negligible. Here, if the difference was of the order of 1/100 eV, it was neglected altogether; otherwise, the different values have been reported, as an indication of the uncertainty that may be associated with the calculation of that specific quantity.

In addition to characteristic energies, in the case of self-interstitial type defects the vibrational entropy of formation has been calculated, as well. The calculation was performed in the harmonic approximation, by diagonalising the dynamic matrix, as detailed in [11]. Finally, for single point-defects the formation volume has been estimated by performing a constant pressure relaxation, i.e. by minimizing the energy also with respect to the cell geometry.

A few words are necessary concerning the reference data used for comparison. Experimental values for characteristic energies of defects are scarce and limited to single point-defects. In all other cases, the only possible reference data for comparison are those from DFT calculations. While these are clearly more reliable than empirical potential data and are supposed to be *ab initio*, i.e. not to require the use of fitted parameters, quantitative differences in the results nevertheless exist, depending on the used DFT approximations. The values reported here, for all of which a precise reference is given (values calculated as part of this work have been

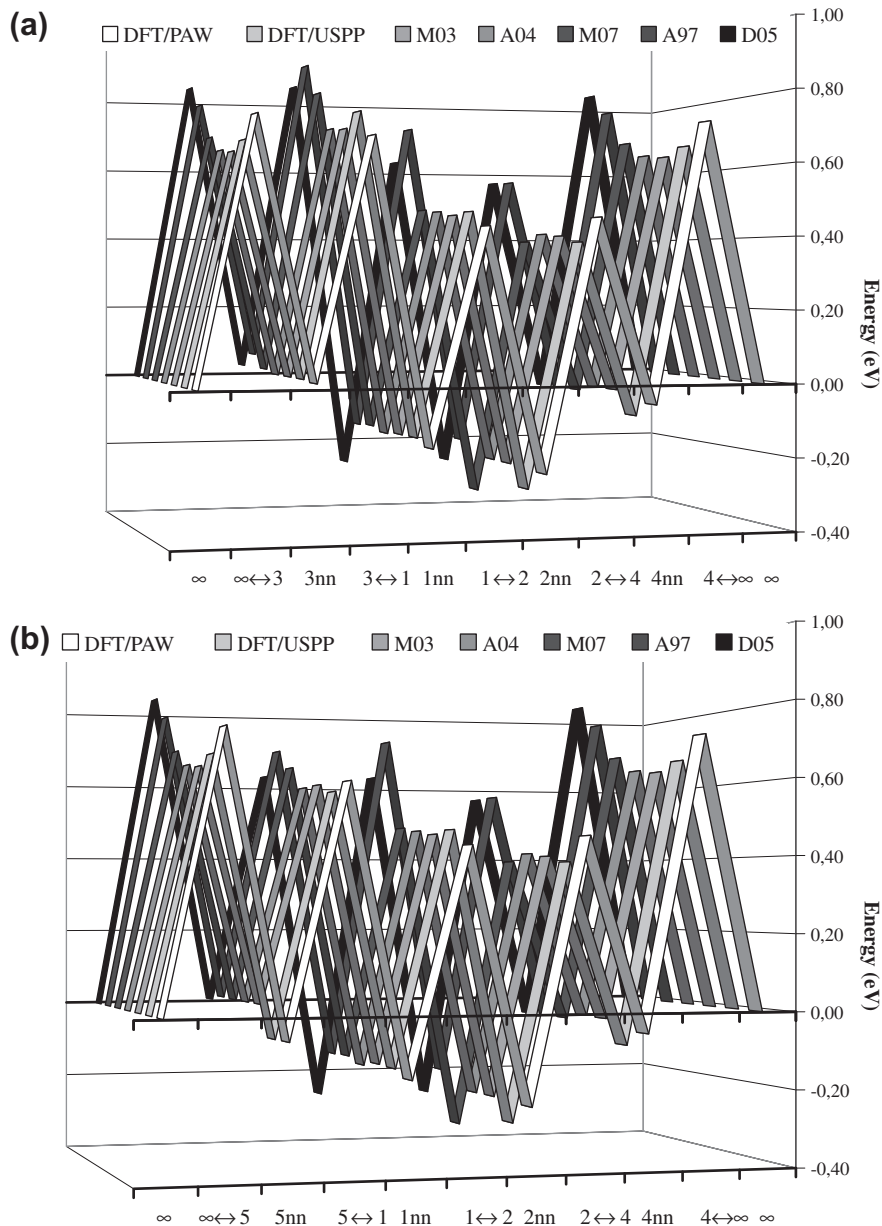


Fig. 6. Simplified energy landscape seen by the second vacancy of a di-vacancy (see Fig. 3) according to the different potentials and to DFT: (a) from 3rd nearest neighbour (left) to 4th nearest neighbour (right) and (b) from 5th nearest neighbour (left) to 4th nearest neighbour (right). For the differences between DFT methods, see Section 3.1.

always performed according to published methodology), have been obtained either with the SIESTA code [4,23,49], or with the VASP code [50]. In the SIESTA code valence electrons are described as linear combinations of numerical pseudoatomic orbitals using a basis set of localised functions. Core electrons are replaced by non-local norm-conserving pseudopotentials and the calculations were performed using the generalised gradient approximation (GGA) functional proposed by Perdew et al. [51]. In contrast, VASP is a plane-wave code in which the core part of valence electrons can be represented using either the projector-augmented wave (PAW) approach [52,53], or ultra-soft pseudo potentials (USPP) [54,55]. The calculations were performed using the GGA functional of Perdew et al. [56]. PAW calculations are more accurate than USPP calculations, especially for magnetic materials, and most VASP reference data reported here have been obtained with this method. Nonetheless, USPP have been extensively used as well in the past and some of the reference values reported here have been indeed calculated in this way, too. In turn, plane-wave codes are more accurate than pseudoatomic orbitals codes such as SIESTA, which are, however, faster for many applications and for this reason have been, and still are, widely used. Thus, a large number of reference data reported here has been produced using SIESTA, too. In most cases, particularly when it comes to binding and migration energies, the difference between using one code or another, one approach or another, is qualitatively (and largely also quantitatively) negligible. In a few cases, however, the discrepancy can be significant, as will be seen. Thus, also the reference data must be taken with care, by not forgetting that they, too, are affected by uncertainties, such a consideration including of course also experimental measurements.

Dynamic calculations are of use especially in order to estimate the effective migration energy of point-defects and their clusters, allowing for all possible migration mechanisms, as well as possible entropy effects. They are, however, computationally heavy, often too heavy to be affordable. For this reason in this comparison exercise only a limited number of dynamic migration energies is reported. The calculation method may vary significantly and therefore in each case the reader is referred to the specific work for details. A few calculations were performed expressly for this work, namely for the self-interstitial migration energy with A04, D05 and M07. In these, the number of self-interstitial jumps was dynamically determined as $N_j = \langle R^2 \rangle / r_{1nn}^2$ [57], where $\langle R^2 \rangle$ is the mean square displacement, obtained as sum of the displacements of all atoms in the simulation cell during the simulated time in a long run (this approach has the advantage that one does not need to define and track defect positions), and r_{1nn} is the 1st nearest neighbour distance (jump distance). Both pressure and temperature control were used in the simulation; simulations without this control revealed only a small effect of 0.5% variation on the results for the activation energy. No correlation factor was used in the calculations, but if a constant factor is assumed in the temperature range of interest (in this case 300–600 K), the activation energy would not be affected; if, on the other hand, the factor grew with temperature, the energy would shift slightly upwards.

3.2. Vacancy-type defects

Tables 2 and 3 compare the descriptions given by the different potentials for small vacancy-type defects in terms of, respectively, formation and binding energies (Table 2), and migration energies (Table 3). In addition to the single-vacancy, clusters of up to four

Table 4
Properties of single SIA configurations in Fe (formation energies, volumes and entropies), as predicted by the different potentials in static calculations, compared with either experimental or, more often, *ab initio* (in italics) data. Legend: E^{for} , V^{for} and S^{for} stand for formation energy, volume and entropy, respectively (V^{for} is expressed in units of atomic volume, $\Omega_0 = a_0^3/2$; S^{for} is calculated at constant volume [11] and expressed in units of Boltzmann's constant, k_B); (ijk) denote the orientation of the dumbbell or crowdion; *TET* and *OCT* stand for tetrahedral and octahedral interstitial position, respectively; N/A not available. For the differences between DFT methods, see Section 3.1.

Description	A97	M03	A04	D05	M07	Exp. and/or <i>ab initio</i>
$E_{(110)}^{for}$ (eV)	4.87 ^{a,b} , 4.70 ^c	3.50 ^b , 3.53 ^d	3.53, 3.57, 3.59 ^e	3.65 ^{b,f}	3.69, 3.73	4.7–5 ^g , 3.64 ^h , 3.77 ⁱ , 3.94 ^j , 3.64–4.03 (range depending on used DFT method) ^k
$V_{(110)}^{for}$ (Ω_0)	0.76 ^{a,b}	0.21, 0.22 ^b	0.25	–0.57 ^b	0.50	N/A
$S_{SIA(110)}^{for}$ (k_B)	–11.05 ^l	1.41 ^l	2.8 ^l	–21.0 ^l	–1.9	N/A
$E_{(111)}^{for}$ (eV)	5.00 ^a , 5.01 ^b , 4.83 ^c	3.99 ^b , 4.02 ^d	4.00, 4.01, (constrained, otherwise becomes $\langle 110 \rangle$) ^d	4.24 ^{b,f} (dumbbell), 4.13 (crowdion)	4.36, 4.39	4.34 ^j , 4.49 ^h , 4.34–4.72 (depending on used DFT method) ^k
$V_{(111)}^{for}$ (Ω_0)	0.64 ^a	–0.03	–0.001	–0.34	0.29	N/A
$S_{SIA(111)}^{for}$ (k_B)	–4.15 ^l	4.41 ^l	9.6 ^l	Unstable ^l	6.4	N/A
E_{TET}^{for} (eV)	5.63	4.16 ^d	4.15	4.29	4.31	4.28 ⁱ
$E_{(100)}^{for}$ (eV)	6.10 ^b (constrained, otherwise unstable)	4.33 ^c	4.32 ^b , 4.34 (constrained, otherwise becomes Oct) ^d	4.58 ^b , 4.60 ^f (constrained, otherwise becomes Oct) ^c	4.76, 4.78	4.80 ^h , 5.04 ^j , 4.64–5.13 (depending on used DFT method) ^k
$S_{SIA(100)}^{for}$ (k_B)	Unstable ^l	2.73 ^l	1.8 ^l	Unstable	–2.0	N/A
E_{OCT}^{for} (eV)	6.00	4.19 ^d	4.17, 4.22 ^e	4.48 ^f	4.90	4.97 (unstable) ^j
$\Delta E_{(111)-(110)}$ (eV)	0.13 ^{a,c} , 0.14 ^b	0.49 ^{b,d}	0.44 ^{a,c} , 0.47	0.59 ^{b,f} (dumbbell versus dumbbell), 0.49 (crowdion versus dumbbell) ^c	0.68	0.70 ^h , 0.72 ^j , 0.70–0.72 (depending on used DFT method) ^k

^a Ref. [24].

^b Ref. [37].

^c Version of the potential modified at short distances (A. Serra, unpublished work).

^d Ref. [4].

^e Ref. [6].

^f Ref. [22].

^g Ref. [71].

^h Ref. [23].

ⁱ This work, DFT/SIESTA (see [4] for calculations details).

^j Ref. [3].

^k Ref. [60].

^l Ref. [11].

^m Ref. [7].

vacancies are considered. Fig. 3 depicts the possible configurations for the di-vacancy and the possible transitions between configurations (the configurations for the tri- and tetra-vacancy are depicted directly on Table 2). Fig. 4 summarises the binding energy landscape as a function of di-vacancy configuration (upper panel) and vacancy-cluster size (lower panel). Fig. 5 shows the energy profile followed by the single-vacancy during a diffusion jump (i.e. exchange of position with a 1st nearest neighbour atom) according to the different potentials and DFT. Finally, Fig. 6 provides a simplified energy landscape for the process of di-vacancy migration (only the energy of the possible configurations and the saddle points of the transitions between them are represented).

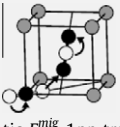
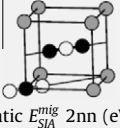
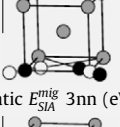
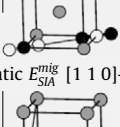
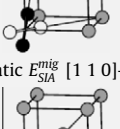
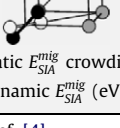
The vacancy formation energy is underestimated by all potentials, except M07 and – to a lesser extent – D05, as compared to DFT (large uncertainty exists concerning the experimental value). The binding energies of small clusters (Table 2 and Fig. 4) are rea-

sonably well reproduced by all potentials, although none reproduces the relatively strong binding for the di-vacancy at 4th and 5th nearest neighbour distances and D05 generally overestimates the binding, particularly for the 1st nearest neighbour di-vacancy configuration, which is as tightly bound as the 2nd nearest neighbour one (ground state).

The migration energy of the vacancy tends to be overestimated by potentials as compared to DFT and even more as compared to experiment, the best performance being given by M03 and A04 (Table 3). The latter are also the potentials that reproduce most closely the energy barrier landscape for the migration of the di-vacancy, as compared to DFT (Fig. 6). However, these two potentials (as well as D05) predict a double-humped energy profile for the vacancy migration (Fig. 5), which is physically of unclear significance and does not appear in the DFT calculation (this problem is removed in M07 and hardly appears in A97).

Table 5

Migration energy of single SIA (E_{SIA}^{mig}) in Fe, according to the different potentials, compared with either experimental or, more often, *ab initio* (in italics) data. Values have been statically calculated for each possible mechanism (pictorially described and numbered from 1 to 6), as well as for crowdion. Dynamically calculated values (effective values) are also provided. N/A stands for not available.

Description	A97	M03	A04	D05	M07	Exp. and/or <i>ab initio</i>
Static E_{SIA}^{mig} (eV) (main jump mechanism) (1) 	0.18	0.31 ^a	0.31 (static), 0.304 (dimer method) ^b	0.26, 0.32 ^c	0.29	0.30 ± 0.03 ^d , 0.34 ^e
Static E_{SIA}^{mig} 1nn transl. (eV) (2) 	0.17	0.44 ^a	0.46	0.49	0.64	0.78 ^e
Static E_{SIA}^{mig} 2nn (eV) (3) 	0.75	0.64 ^a	0.61	0.73	0.61	0.50 ^e
Static E_{SIA}^{mig} 3nn (eV) (4) 	1.14	0.70 ^a	0.57	0.84	1.22	1.18 ^e
Static E_{SIA}^{mig} [1 1 0]–[0 1 1] rotation (eV) (5) 	0.23	0.43 ^a	0.45	0.39	0.50	0.56 ^e
Static E_{SIA}^{mig} [1 1 0]–[1 1 1] rotation (eV) (6) 	0.16 (dimer method) ^f , 0.17	0.50 ^a	0.52	0.59	0.68	0.72, 0.76 ^e
Static E_{SIA}^{mig} crowdion glide (eV)	0.002 (dimer method) ^f	0.003	0.003	0.004	0.002	N/A
Dynamic E_{SIA}^{mig} (eV)	0.055 ^h , 0.127 ⁱ	N/A ^l	0.26 ± 0.01 ^j , 0.27, 0.31 ^k	0.25 ± 0.01 ^j	0.27 ± 0.01 ^l	0.30 ± 0.03 ^d

^a Ref. [4].

^b Ref. [72].

^c Ref. [22].

^d Refs. [73–75].

^e Ref. [23].

^f Ref. [76].

^gThis work, SIESTA (see [4] for calculations details).

^h Ref. [77].

ⁱ Ref. [27].

^j This work (see text), using method from [57].

^k Ref. [8].

^l Expected to be coincident with A04.

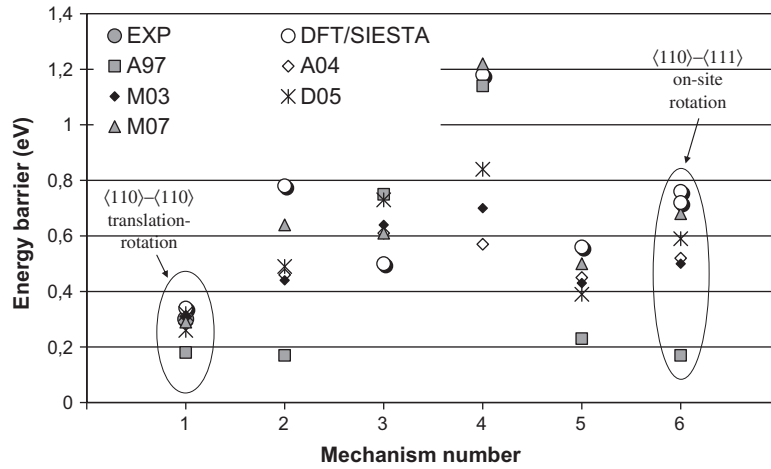
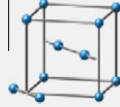
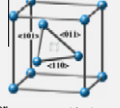


Fig. 7. Summary of statically calculated energy barriers corresponding to mechanisms (1)–(6) (see Table 5).

Table 6
Properties of di-SIA configurations in Fe (formation energies and entropies, migration energies), as predicted by the different potentials in both static and dynamic calculations, compared with either experimental or, more often, *ab initio* (in italics) data. Legend: E^{for} and S^{for} stand for formation energy and entropy, respectively (S^{for} expressed in units of Boltzmann's constant, k_B); (ijk) denotes the orientation of the configuration (pictorially represented for better clarity), NPC stands for non-parallel configuration [12]; N/A not available. For the differences between SIESTA and VASP–PAW, see Section 3.1.

Description	A97	M03	A04	D05	M07	Exp. and/or <i>ab initio</i>
$E_{di-SIA(110)}^{for}$ (eV)	8.57	6.14, 6.21 ^a , 6.31	6.21, 6.23 ^b , 6.29, 6.31	6.42, 6.45	6.30	6.99 (SIESTA) ^c , 7.15 (VASP–PAW) ^c
 $S_{di-SIA(110)}^{for}$ (k_B)	–15.29 ^d	2.06 ^d	3.7 ^c , 4.0 ^d	–32.1 ^d	–3.6	N/A
$E_{di-SIA(111)}^{for}$ (eV)	8.58	6.84 ^a	6.74 ^b	6.95	7.31	7.74 (SIESTA) ^c
 $S_{di-SIA(111)}^{for}$ (k_B)	–10.16 ^d	10.03 ^d	11.4 ^{c,d}	–23.6 ^d	1.2	N/A
$E_{di-SIA_{NPC}}^{for}$ (eV)	8.73	6.49, 6.61	6.51, 6.54 ^c , 6.58	6.76, 6.79	6.41	6.95 (SIESTA) ^c , 7.04 (VASP–PAW) ^c
$S_{di-SIA_{NPC}}^{for}$ (k_B)	–20.6	10.2	10.2 ^c	–13.2	0.5	N/A
$E_{di-SIA(100)}^{for}$ (eV)	Unstable (turns to $\langle 111 \rangle$)	6.67 ^a , 6.69, unstable (turns to $\langle 211 \rangle$) ^a	6.70, unstable (turns to $\langle 211 \rangle$) ^a	Unstable	6.80	7.10 (SIESTA) ^a
$S_{di-SIA(100)}^{for}$ (k_B)	Unstable ^d	3.92 (value for $\langle 211 \rangle$ config.) ^d	4.73 (value for $\langle 211 \rangle$ config.) ^d	–38.5 (for metastable config. which has no $\langle 100 \rangle$ orientation) ^d	–2.3	N/A
E_{di-SIA}^{mig} (eV) (static)	0.16 ($\langle 110 \rangle$ config.)	0.31 ^a	0.31 ($\langle 110 \rangle$ config.), 0.34/0.55 (one jumps after the other / the two jump together)	0.26 ($\langle 110 \rangle$ config.)	0.33 ($\langle 110 \rangle$ config.)	0.42 ^e , 0.43 ^f (static for $\langle 110 \rangle$ config.)
E_{di-SIA}^{mig} (eV) (dynamic)	0.084 ^g	N/A ^h	0.31, 0.33 ^b	N/A	N/A	~0.42 ⁱ

^a Ref. [4].

^b Ref. [8].

^c Ref. [12].

^d Ref. [11].

^e Ref. [23].

^f Ref. [63].

^g Ref. [27].

^h Expected to be the same as for A04.

ⁱ Ref. [75] (based on interpretation of resistivity recovery data).

It is worth mentioning here that different methods for the obtainment of the vacancy migration energy profile (i.e. drag method [65] versus nudged elastic bands (NEB) [65,66], slightly different choices of initial and final conditions, different accuracy in the relaxation, ...) have been observed to lead to somewhat different paths, particularly at the two extremes; however, the saddle point and the energy profile in the region of the saddle point are generally found to be independent of the used calculation method.

3.3. Self-interstitial-type defects

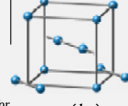
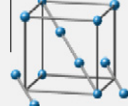

Tables 4 and 5 provide a detailed account of the description that each potential gives for, respectively, the different configurations and migration mechanisms of the single SIA (the configurations are dumbbells, i.e. two atoms sharing the same lattice site, oriented in the specified crystallographic direction; the considered migration mechanisms are pictorially represented directly in Table 5). The migration energy values per mechanism and potentials are also summarised in Fig. 7. Tables 6–8 contain the properties predicted for the different possible configurations of, respectively, di-SIA, tri-SIA, and tetra- and penta-SIA together (the configurations are depicted on the tables themselves). Finally, Fig. 8 shows the relative stability of the different configurations with respect to the (supposed) ground state, i.e. parallel $\langle 110 \rangle$ dumbbells, as a function of cluster size. The chosen configurations correspond in general to parallel dumbbells, oriented along three crystallographic directions, namely $\langle 110 \rangle$, $\langle 111 \rangle$ and $\langle 100 \rangle$. The first seems the most natural choice, because the stable single SIA is a $\langle 110 \rangle$

dumbbell. However, experimentally it is long known that interstitial loops in iron have either a $\langle 111 \rangle$ or a $\langle 100 \rangle$ orientation [78]. For this reason, these are the orientations typically studied (see e.g. [4]). However, it has been recently discovered that SIA clusters can be stable also in configurations where the dumbbells are not parallel [12]. These non-parallel configurations (NPCs), as discussed in [12,79], have a number of peculiarities and are deemed to be of importance for a more correct description of the microstructure evolution in iron and iron alloys under irradiation.

The largely improved description of self-interstitials as compared to DFT is the strong point of the most recent potentials (M03, A04, D05 and M07) when compared to the older A97. The four of them reproduce correctly the sequence of stability of the different single SIA configurations (Table 4), although with non-negligible quantitative discrepancies, particularly for the tetrahedral configuration (Fig. 8B). However, D05 exhibits the oddity of predicting a negative volume of formation for the single SIA. The four potentials reproduce also satisfactorily, with only subtle differences, the relative stability of $\langle 111 \rangle$ versus $\langle 110 \rangle$ configurations, M03 and A04 being overall the closest to DFT (Fig. 8A). The relative stability of non-parallel configurations (NPCs) is, however, generally not satisfactorily reproduced (Fig. 8B): no potential predicts, for example, the DFT fact that the NPC is the ground state for the di-SIA. For larger NPC clusters, important discrepancies exist even between DFT methods [12], this being the most flagrant example that also reference DFT data must be taken with care, as anticipated in Section 3.1. If VASP/PAW results are taken as the most reliable ones, we see that, by chance, D05 predicts the correct

Table 7

Properties of tri-SIA configurations in Fe (formation energies and entropies, migration energies), as predicted by the different potentials in both static and dynamic calculations, compared with *ab initio* (in italics) data.

Description	A97	M03	A04	D05	M07	<i>Ab initio</i>
$E_{\text{tri-SIA}\langle 110 \rangle}^{\text{for}}$ (eV)	12.13	8.85, 9.03 ^a	8.84, 8.87 ^b , 9.00, 9.04 ^a	9.15, 9.22 ^a	8.95	9.81 (SIESTA) ^c , 10.25 (VASP/PAW) ^c
						
$S_{\text{tri-SIA}\langle 110 \rangle}^{\text{for}}$ (k_B)	-17.15 ^d	3.12 ^d	5.0 ^c , 5.4 ^d	-42.9	-3.5	N/A
$E_{\text{tri-SIA}\langle 111 \rangle}^{\text{for}}$ (eV)	11.37 ^e , 11.83	9.31, 9.37 ^f	9.28, 9.36 ^b , 9.38	9.31	9.41	10.17 (SIESTA) ^c
						
$S_{\text{tri-SIA}\langle 111 \rangle}^{\text{for}}$ (k_B)	-12.65 ^d	17.23 ^d	19.7 ^{c,d}	-25.3 ^d	10.1	N/A
$E_{\text{tri-SIA_NPC}}^{\text{for}}$ (eV)	12.53	9.53, 9.81 ^a	9.60, 9.66 ^c , 9.75 ^a	9.80, 9.85 ^a	9.21	10.48 (SIESTA) ^c , 10.19 (VASP/PAW) ^c
						
$S_{\text{tri-SIA_NPC}}^{\text{for}}$ (k_B)	-24.7	13.0	15.0 ^c	-26.4	6.2	N/A
$E_{\text{tri-SIA}\langle 100 \rangle}^{\text{for}}$ (eV)	12.10	10.53 ^f	10.54	Unstable (turns to $\langle 110 \rangle$)	10.05	11.43 (SIESTA) ^f
$S_{\text{tri-SIA}\langle 100 \rangle}^{\text{for}}$ (k_B)	Unstable ^d	6.39 ^d	14.0 ^d	-38.6 ^d (not in $\langle 100 \rangle$ config.)	-2.3	N/A
$E_{\text{tri-SIA}}^{\text{mig}}$ (eV)	0.074 (dynamic) ^g	N/A	0.14 ^b , 0.15 (both values dynamic)	N/A	N/A	0.43 (static for $\langle 110 \rangle$ config.) ^h

Legend: see Table 6 caption.

^a 250 atoms.

^b Ref. [8].

^c Ref. [12].

^d Ref. [11].

^e Version of the potential modified at short distances (A. Serra, unpublished work).

^f Ref. [4].

^g Ref. [27].

^h Ref. [63].

stability for the tetra-SIA NPC and M07 (as well as A97) assign to this configuration the role of ground state, in qualitative agreement with the message conveyed by the VASP/PAW values. However, the supposedly correct trend is never reproduced. Concerning $\langle 100 \rangle$ configurations, these clusters are difficult to stabilise, both using potentials and DFT, so it is difficult to draw conclusions and any way these would be of unclear significance. The different case of large $\langle 100 \rangle$ versus $\frac{1}{2}\langle 111 \rangle$ SIA clusters (loops) is addressed in Section 4.2. Overall, it appears clear that the study of SIA-type defects poses more problems than that of vacancies, because they may exist in different configurations and orientations, not always sufficiently stable to be easily and reliably analysed. Their relaxation must be performed with care and small differences in the used procedure may lead to relatively large discrepancies. It is therefore not surprising that, in the tables devoted to these defects, the largest amount of different reported values for the same quantity is found.

Concerning migration mechanisms, the energy barriers for those studied here are best reproduced by M07, but all most recent potentials provide overall good predictions. In particular, the main migration mechanism, i.e. translation-rotation of the $\langle 110 \rangle$ dumbbell (mechanism 1), has a correct barrier with all of them (note difference with respect to A97) and the on-site rotation of the $\langle 110 \rangle$ to the $\langle 111 \rangle$ crowdion (mechanism 6) is not expected to occur according to any of them, except at extremely high temperature (contrary to the prediction of the older A97). Note also that all ex-

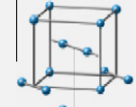
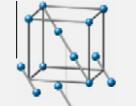
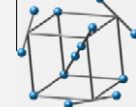
cept A97 predict the correct value (versus DFT) also for the on-site rotation between different $\langle 110 \rangle$ directions (mechanism 5), though not for the jump to 2nn (mechanism 3). A04 may allow at high temperature mechanisms that should not occur (parallel translation to 1nn position of the $\langle 110 \rangle$ dumbbell, mechanism 2), and $\langle 110 \rangle$ jump to 3nn position, mechanism 4), but the improvement with respect to A97, which allows almost all mechanisms, is clear. A detailed discussion of the migration energy of clusters would be out of the scope of the present work and the interested reader is referred for this to [8,12] and to the extensive literature cited therein.

4. Dislocations

4.1. Dislocation lines

The properties of dislocation lines are determined by a relatively large number of parameters and an exhaustive study, which should *a priori* include also dynamic and temperature-dependent analyses, is well beyond the scope of the present work. Here we limit ourselves to a few quantities of some importance that can be calculated in a standard way and can therefore be easily compared, namely the core structure of the screw dislocation (in Fig. 9); the so-called γ -line, i.e. the energy profile when two

Table 8
Properties of tetra- and penta-SIA configurations in Fe (formation energies and entropies, migration energies), as predicted by the different potentials in both static and dynamic calculations, compared with *ab initio* (in italics) data.

Description	A97	M03	A04	D05	M07	<i>Ab initio</i>
$E_{tetra-SIA\langle 110 \rangle}^{for}$ (eV)	14.24 ^a , 15.04	10.81 (after “shaking” at finite temperature), 11.05 ^b	11.05 ^c , 11.04	11.47	10.94	12.31 (SIESTA) ^d , 13.30 (VASP/PAW) ^d
						
$S_{tetra-SIA\langle 110 \rangle}^{for}$ (k _B)	-23.11 ^e	7.81 ^e	9.7 ^{c,e}	-43.8 ^e	0.5	N/A
$E_{tetra-SIA\langle 111 \rangle}^{for}$ (eV)	13.73 ^a , 14.31	11.36 ^b	11.18, 11.22 ^c	11.30	11.74	12.42 (SIESTA) ^d
						
$S_{tetra-SIA\langle 111 \rangle}^{for}$ (k _B)	-17.42 ^e	13.78 ^e	15.9 ^{d,e}	-35.7 ^e	10.6	N/A
$E_{tetra-SIA_NPC}^{for}$ (eV)	14.03	11.14	11.30 ^e	11.52	10.83	12.89 (SIESTA) ^d , 13.37 (VASP/PAW) ^d
						
$S_{tetra-SIA_NPC}^{for}$ (k _B)	-30.3	22.60	22.6 ^d	-35.1	9.3	N/A
$E_{tetra-SIA\langle 100 \rangle}^{for}$ (eV)	Unstable	12.14 ^b	12.04	12.15	12.79	13.38 (SIESTA) ^b
$S_{tetra-SIA\langle 100 \rangle}^{for}$ (k _B)	Unstable ^d	6.24 ^e	16.0 ^e	-57.3 ^e	1.8	N/A
$E_{penta-SIA\langle 110 \rangle}^{for}$ (eV)	Unstable	13.25 ^b	13.42 ^c	13.36	13.47	14.18 (SIESTA) ^b
$S_{penta-SIA\langle 110 \rangle}^{for}$ (k _B)	Unstable ^e	11.37 ^e	15.2 ^e	-52.2 ^e	1.9	N/A
$E_{penta-SIA\langle 111 \rangle}^{for}$ (eV)	16.93	13.36 ^b	13.49 ^c	13.11	13.83	13.88 (SIESTA) ^b
$S_{penta-SIA\langle 111 \rangle}^{for}$ (k _B)	-19.21 ^e	20.01 ^e	22.0 ^e	-36.3 ^e	9.5	N/A
$E_{penta-SIA\langle 100 \rangle}^{for}$ (eV)	20.83	15.49 ^b	15.44	15.66	16.77	16.45 (SIESTA) ^b
$S_{penta-SIA\langle 100 \rangle}^{for}$ (k _B)	-25.23 ^d	12.07 ^d	15.2 ^d	-69.3 ^d	4.5	N/A

Legend: see Table 6 caption.

^a Version of the potential modified at short distances (A. Serra, unpublished work).

^b Ref. [4].

^c Ref. [8].

^d Ref. [12].

^e Ref. [11].

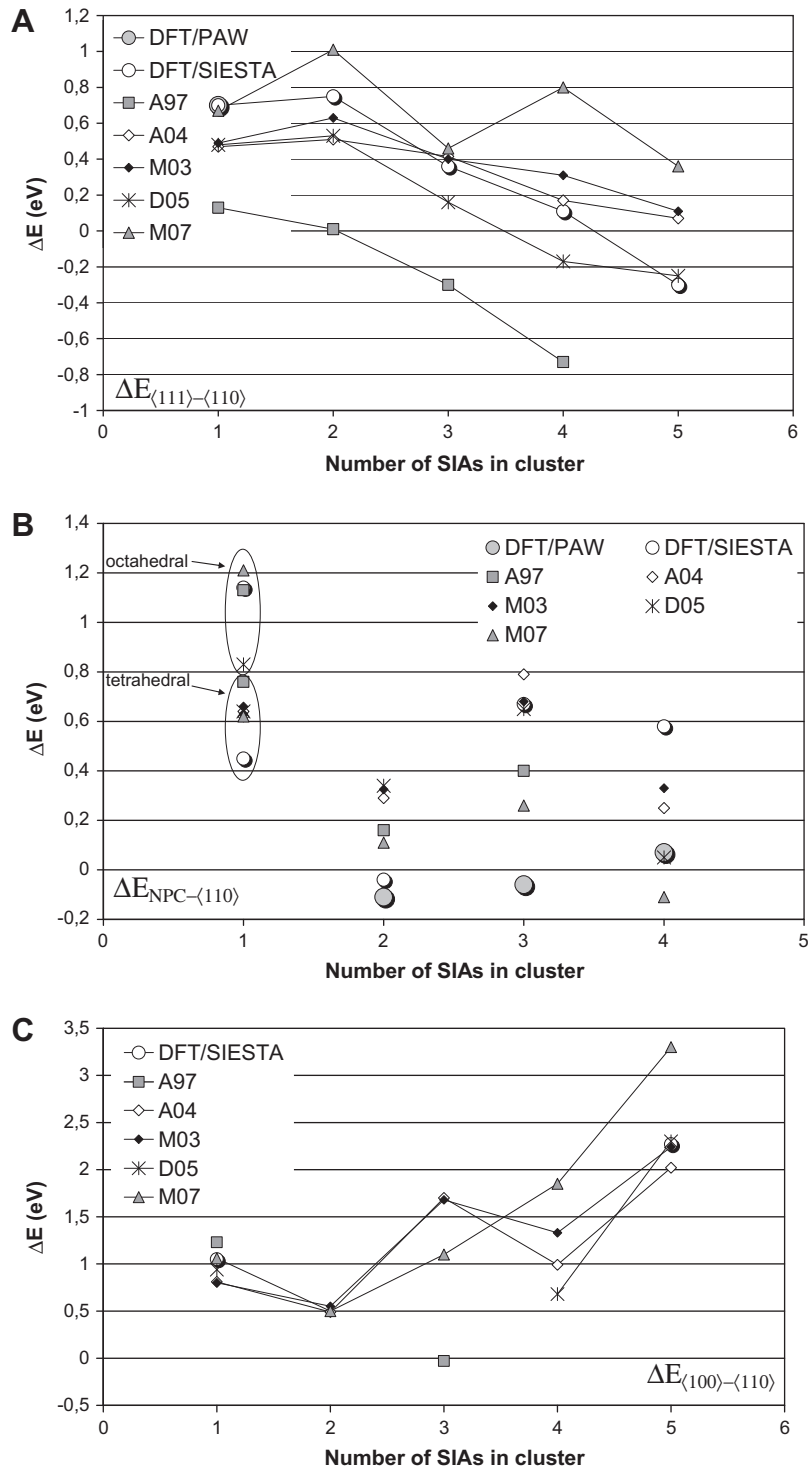


Fig. 8. Formation energy difference (ΔE) of: (A) $\langle 111 \rangle$ configurations, (B) non-parallel configurations (NPC) and (C) $\langle 100 \rangle$ configurations, with respect to the reference $\langle 110 \rangle$ configurations. For the differences between DFT methods, see Section 3.1.

adjacent atomic planes are made to glide rigidly one respect to the other (generalised stacking fault energy, in Fig. 10); and the dislocation strain energy as a function of the radial distance from the dislocation line, i.e. the elastic energy stored in cylinders of growing radius whose axis is the dislocation line itself (in Fig. 11).

In Fig. 9 the core structure of the screw dislocation, as predicted by the different potentials and by DFT calculations performed using VASP/PAW, is shown in Vitek's representation [80]. Accord-

ing to this representation, the crystal is looked at from the $\langle 111 \rangle$ direction, i.e. the atomic plane represented is normal to the dislocation line, thereby appearing as a triangular network. The length of the arrows joining the vertices of the triangles, that represent in fact atomic $\langle 111 \rangle$ columns, is proportional to the disregistry (difference between actual and perfect-lattice interplane spacing as fraction of the perfect-lattice interplane spacing) between the concerned atomic columns. (Note that the atoms at each of the

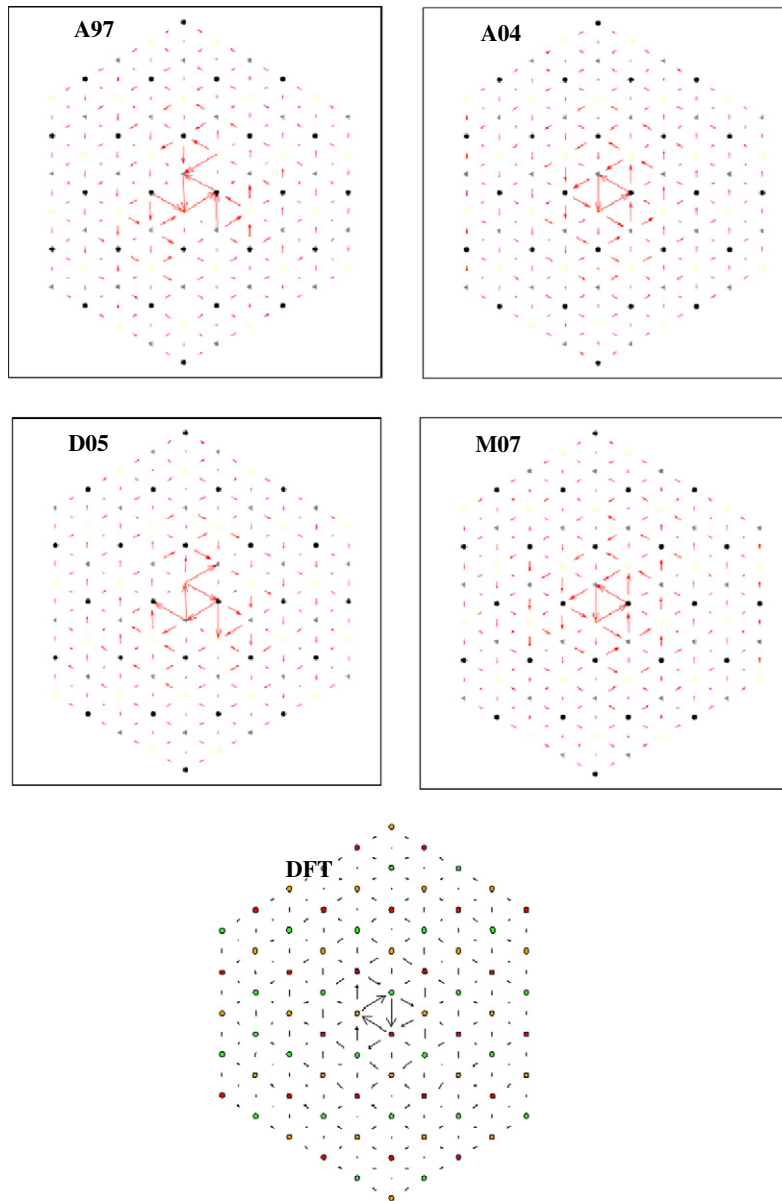


Fig. 9. Screw dislocation core according to four potentials and as calculated by DFT (VASP, PAW), in the Vitek's representation [80]. Only Mendelev-type potentials predict a compact core consistent with DFT (VASP/PAW) indications (M03 provides results coincident with A04 [5]).

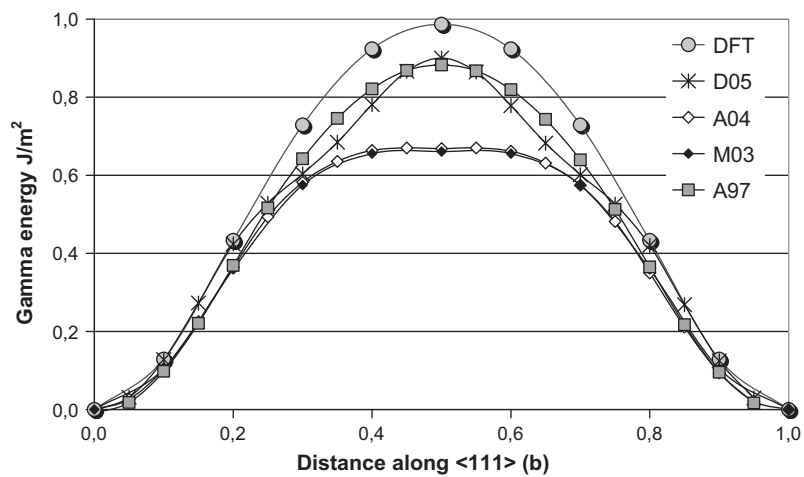


Fig. 10. Gamma energy of (1 1 0) plane along the Burgers vector ($b = \frac{1}{2}[1 1 1]$) according to four potentials and DFT (VASP/PAW). Significant differences exist.

vertices of the same triangle lie in fact on different parallel atomic planes.) The triangle formed by the longest arrows, i.e. the largest disregistry, identifies the screw dislocation core. It can be seen that the core is compact, or non-degenerate, as in DFT, only according to the Mendeleev-type potentials: A04 and M07. (M03, though not reported here, not only gives the same result as A04, but provided also the first evidence of double kink mechanism for screw dislocation glide in a molecular dynamics simulation [5], reproducing the motion of this type of dislocation on $\{110\}$ planes, in agreement with experiments and theory.) On the other hand, both the older A97 and D05 predict a threefold, spread (or degenerate) core. In partial contrast with this prediction, the Mendeleev-type potentials provide the lowest γ -line (Fig. 10), i.e. require the lowest energy to make two atomic planes shift one respect to the other, significantly less than according to DFT. *A priori*, this should suggest a more pronounced tendency of the dislocation core to spread than with other potentials, but the core structures of Fig. 9 suggest exactly the opposite. Thus, the relationship between these two static results – the only ones for which, however, DFT results can be produced for comparison – is not obvious, as well as it is not obvious how to link them with the actual dynamic behaviour of the dislocation. Dynamically, Mendeleev-type potentials provide sensible results, as demonstrated at least in the case of M03 [5]. Finally, in spite of the clear difference between potentials concerning screw dislocation core description and γ -line, the dislocation strain energy is largely the same for all potentials, with the only exception of a somewhat higher value predicted by D05 for the screw dislocation (as a con-

sequence of a somewhat different core energy). In this case, however, no DFT reference data is available for comparison, as the required simulation volume would be far too large for DFT methods to be applicable.

4.2. Dislocation loops

Dislocation loops are in fact clusters of SIA in the form of platelets of parallel dumbbells (or better said crowdions), large enough to be able to say that, in the central region of the platelet, the crystal is close to being perfect. When this happens, the disturbance is confined to the edge of the platelet, thereby effectively creating a closed edge dislocation line, with Burgers vector normal, or almost normal, to the loop habit plane (the plane of the platelet of parallel dumbbells or crowdions). In iron, two types of loops are observed experimentally: with Burgers vector $\frac{1}{2}\langle 111 \rangle$ and with Burgers vector $\langle 100 \rangle$ [78].

A clearcut size criterion to establish when a cluster of SIA should be better called loop cannot be provided, but a Burgers vector can already be identified in clusters containing 30–40 SIA and already this size is hardly accessible to DFT. Visible loops are even larger and their study therefore requires the use of simulation volumes containing several tens of thousands of atoms, totally inaccessible to DFT. Thus, in the case of loops we have no DFT reference data and for their study we can only rely on potentials,

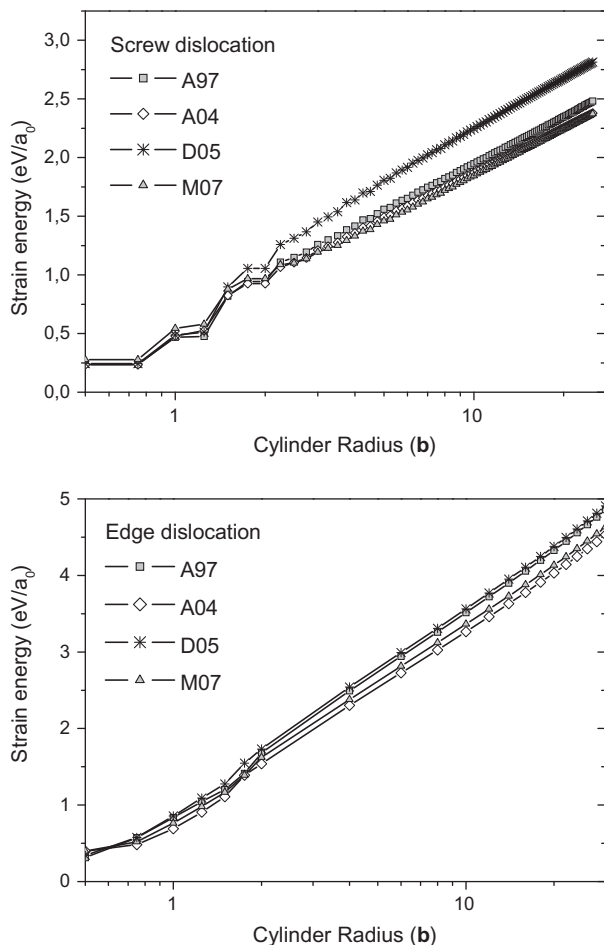


Fig. 11. Strain energy for screw and edge dislocation as a function of the radial distance from the dislocation line according to four potentials.

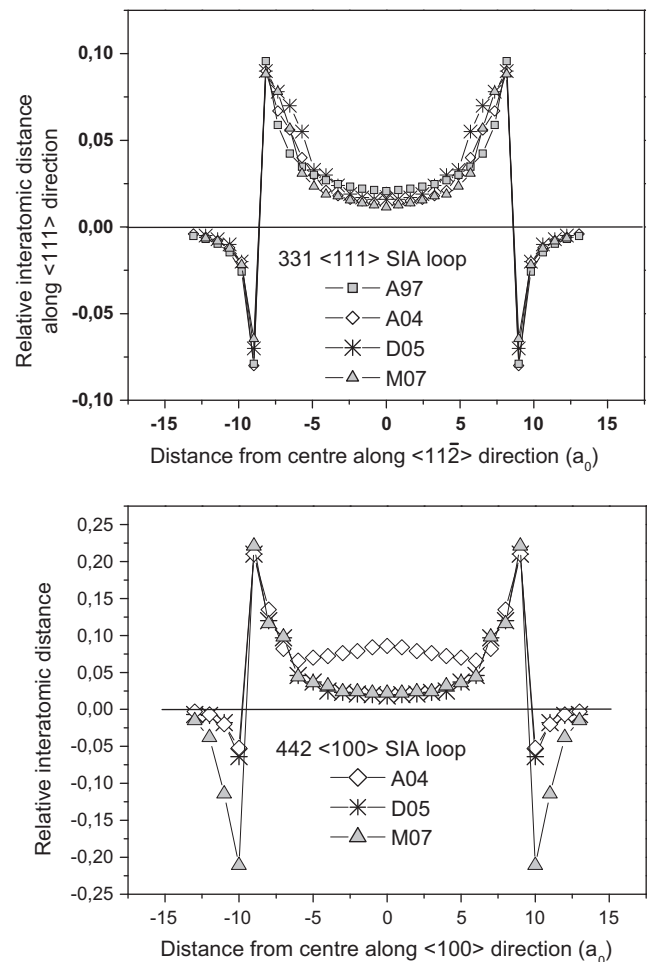


Fig. 12. Strain field of a $\frac{1}{2}\langle 111 \rangle$ loop (above) and a $\langle 100 \rangle$ loop (below) in terms of a dimensional deviation from the equilibrium interatomic distance along the Burgers vector direction on the loop habit plane, in units of lattice parameters ($a_0 \sim 0.287$ nm), calculated with different potentials.

without clear and direct indications to decide which potential is more correct.

As in the case of dislocation lines, the properties of loops are determined by a large number of parameters. Here we report on two only: the strain field at the habit plane, in terms of atomic registry parallel to the loop Burgers vector (Fig. 12), and the formation (or self-) energy versus loop size (Fig. 13). Both these quantities are hardly accessible to experiments, so it is impossible to make any firm conclusion about the relative accuracy of the different potentials. The only considerations that can be made are qualitative. For example, it appears that $\frac{1}{2}\langle 111 \rangle$ loops are very similarly described by all potentials, while discrepancies appear in the description of $\langle 100 \rangle$ loops (Fig. 12). This different description of $\langle 100 \rangle$ loops depending on the potential is reflected also in the formation energies as a function of size (Fig. 12): A97, M03 and A04 provide similar qualitative trends: the $\frac{1}{2}\langle 111 \rangle$ loops are energetically favoured for all sizes, with slight energy differences (negligible with A04) depending on the habit plane of $\langle 100 \rangle$ loops. In D05 the difference between $\langle 100 \rangle$ and $\frac{1}{2}\langle 111 \rangle$

loops is the largest, with no influence of the habit plane of $\langle 100 \rangle$ loops, thereby fully agreeing with the isotropic elasticity theory picture [81]. On the contrary, M07 predicts an inversion of relative stability above a certain size. If this was proven to be true, it would explain the appearance in Fe of $\langle 100 \rangle$ loops. However, experimentally both types of loops are observed for similar sizes [78] and recent work suggests in fact that temperature, more than size, may have an important role in determining the stability of $\langle 100 \rangle$ versus $\frac{1}{2}\langle 111 \rangle$ loops [12,82].

5. Damage production

5.1. Threshold displacement energies

The threshold displacement energy is defined as the minimum energy that must be provided to an atom in order to definitively displace it from its lattice site, so as to form a stable Frenkel pair (FP), i.e. a vacancy and a SIA that do not recombine spontaneously.

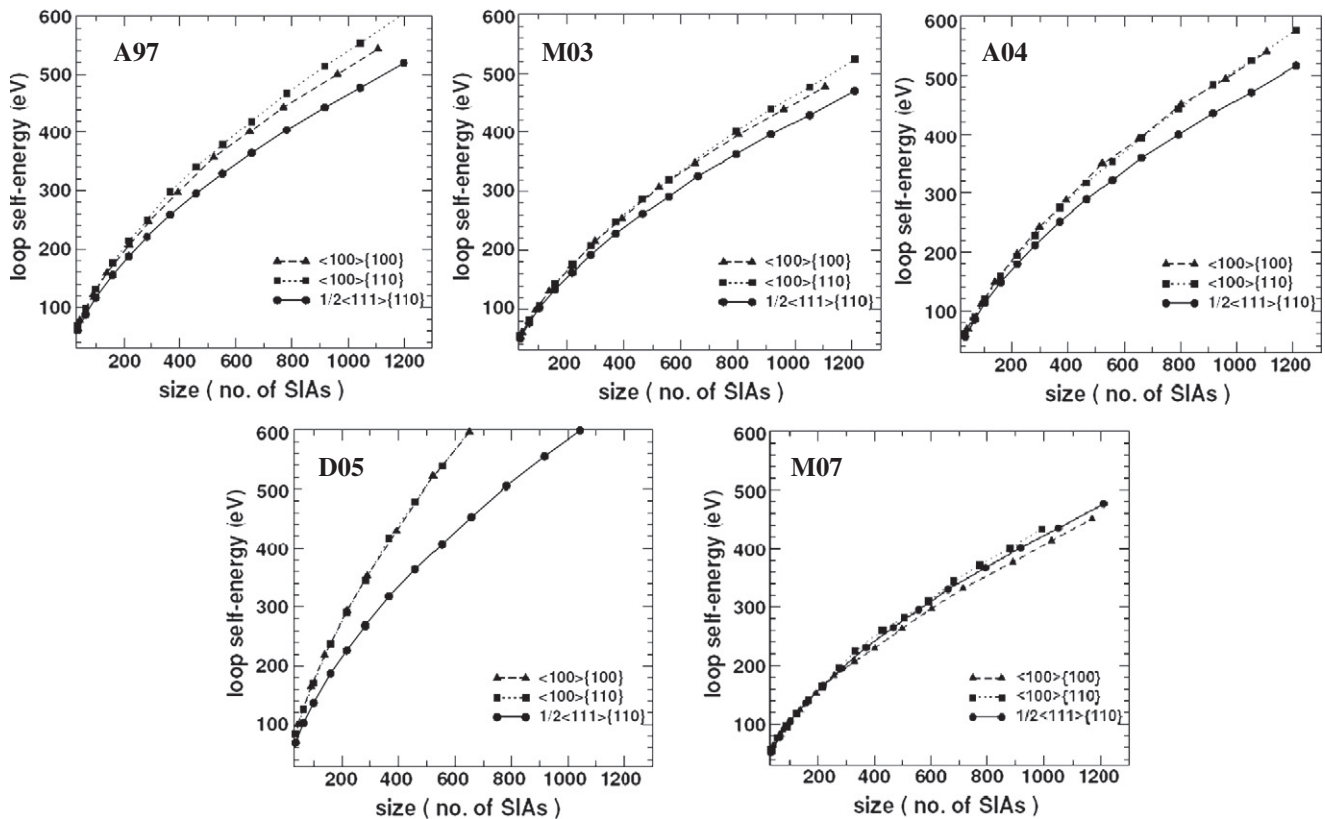


Fig. 13. Loop formation energy versus number of SIAs for different types of loop (Burgers vector and habit plane), with the different potentials, as specified on the graphs.

Table 9
Threshold displacement energies depending on primary knock-on atom (PKA) direction, as well as mean (and median), according to the different potentials. For calculation methodology, see [83].

PKA direction	A97 ^a	M03 ^a	A04 ^a	D05 ^b	M07	Experiment
$\langle 100 \rangle$	17	15	17	33(17)	17	17
$\langle 110 \rangle$	31	27	33	51(29)	33	>30
$\langle 111 \rangle$	35	25	33	35(25)	31	20
Mean (Median) value	44.8 ± 0.4 (41)	36.9 ± 0.1 (35)	39.0 ± 0.3 (35)	66.5 ± 0.5 (35.0 ± 0.4)	37.2 ± 0.5	(40, advised value) ^d

Ref. [84].

^a Ref. [83].

^b Ref. [10] (in parenthesis, value after re-stiffening by Björkas and Nordlund).

^d Refs. [85–87].

Despite its apparent simplicity and clearness, this definition is ambiguous and does not provide a clearcut criterion for the determination of the threshold energy, especially by means of atomistic simulation, because in practice it is never true that above a certain energy value a stable Frenkel pair is *always* produced, and *never* below. This issue has been discussed in [83], where all the possible interpretations of the definition and the difficulties encountered for its application in practice are discussed and an accurate methodology for threshold energy calculation using molecular dynamics

and interatomic potentials is provided. This methodology has been used to produce the data of Table 9.

All potentials (D05 only after re-stiffening, i.e. after modifying the way the equilibrium potential is joined to a more appropriate potential for the treatment of short distance encounters [10]) provide reasonable threshold energies when compared to experimental indications. This, however, is *a priori* only a necessary, not sufficient condition to believe that they are reliable for displacement cascade simulations [88,89].

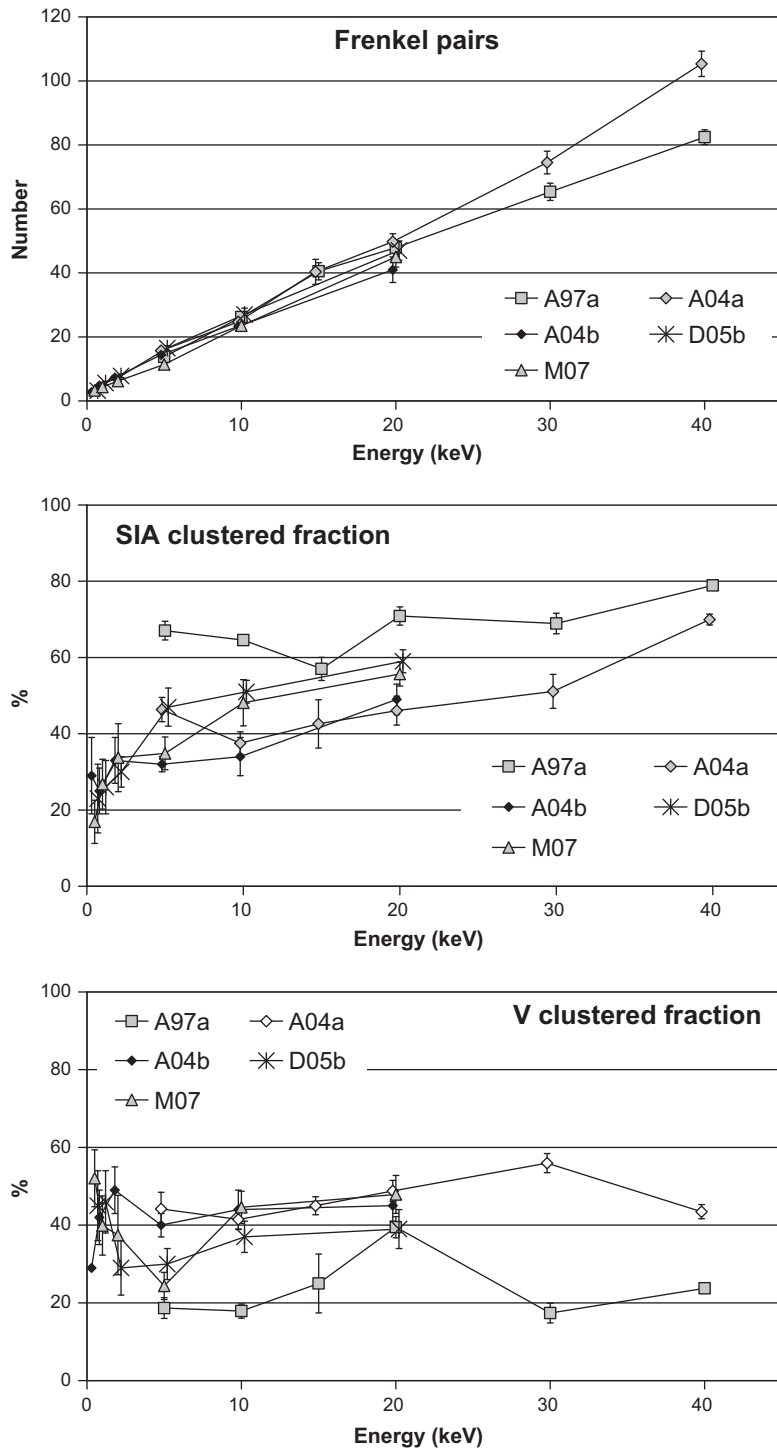


Fig. 14. From top to bottom: number of Frenkel pairs; SIA clustered fraction and vacancy clustered fraction in displacement cascades of different energy simulated by molecular dynamics using some of the potentials here compared. ^aFrom [7]; ^bFrom [10] (same method used to obtain results with M07).

5.2. Displacement cascades

The influence of the interatomic potential on the result of the simulation of displacement cascades (specifically in Fe) has been first studied in [88] and, more recently, in [7] and [10]. A review of results of displacement cascades for Fe is provided in [89]. We refer to these works for the description of the cascade process and of the simulation method. Fig. 14 compares the results obtained with the potentials of interest in this work (all except M03 which is, however, extremely similar to A04 and therefore not expected to provide significantly different results). These are given in terms of: (i) number of FPs left at the end of the cascade process and (ii) fraction of SIA and vacancies found to form clusters after appropriate analysis. As expected [89], no large difference in the number of FPs is observed from one potential to the other except, perhaps, at high energies, where different subcascade production may have a role in determining the number of surviving defects. More pronounced differences emerge in the defect clustered fraction versus cascade energy. Qualitatively, it can be said that the predictions of D05 and M07 are intermediate between A04 (highest clustered vacancy fraction) and A97 (highest clustered SIA fraction). As discussed in [7,88,89], it is impossible to explain the differences between predicted clustered fraction in terms of one or two single factors specific for the used potential. Nonetheless, as shown in [10], it is possible to observe a trend to reduce the scatter when the most recent potentials are used. This convergence of results, which is likely to be the consequence of the fact that these potentials predict similar stability and mobility of SIAs, in addition to having similar repulsive parts, may be interpreted, in itself, as a sign that overall some progress has indeed been made on the path of developing more reliable interatomic potentials for Fe.

6. Concluding remarks

The growth to present-day standards of the speed and efficiency of computers allowed, in the last decade, an impressively large DFT dataset to be produced for defect properties in Fe. This dataset has been partly used here to assess the performance of the most recent interatomic potentials for this metal, as compared to earlier ones, when applied to radiation damage studies. Since these potentials have been fitted having in mind a few key DFT data, unsurprisingly they globally provide results closer than ever to this class of data. Since DFT data are accepted to be highly reliable, this is of course in itself a significant improvement, epitomised by the excellent agreement found, for the first time in the history of MD simulations of Fe, between the dynamically calculated migration energy of the single SIA and its experimental value (Table 5) [8], as well as by the spontaneous prediction of the double kink mechanism for the screw dislocation motion [5]. However, the number of cases in which a direct comparison of interatomic potential results with experimental measurements can be made is limited; so, essentially, what is mainly checked here is how close the interatomic potentials results are to DFT, for cases not considered at all in the fitting procedure. From this point of view, the Mendeleev-type potentials, especially M03 and A04, perform very well, globally much better than, for example, the equally recent and possibly physically more grounded ‘magnetic’ potential, D05. In the latter case, it is necessary to distinguish between the mathematical formalism of D05, which can be interesting in itself and may represent a conceptual improvement, and the accuracy of the fitting that provided the specific set of parameters, which is clearly better in the case of the Mendeleev-type potentials. It is, on the other hand, difficult to make a statement concerning the performance of the bond-order potential developed in [37]: it is certainly attractive to reproduce spontaneously the α - γ transition, but the description

Table 10

Parameters of the M07 potential. The notations are the same as in Ref. [1]. Distances are expressed in Å and energies in eV.

r_1	1.0	a_1^{ϕ} (r_1^{ϕ})	25.762119612643801 (2.3)	a_1^{ψ} (r_1^{ψ})	7.015122199909290 (2.1)
r_2	1.95	a_2^{ϕ} (r_2^{ϕ})	3.842589725515660 (2.4)	a_2^{ψ} (r_2^{ψ})	19.406057935968299 (2.4)
B_0	13.0155822980227	a_3^{ϕ} (r_3^{ϕ})	2.065216917586350 (2.5)	a_3^{ψ} (r_3^{ψ})	-0.213254828113481 (3.2)
B_1	14.6615468843637	a_4^{ϕ} (r_4^{ϕ})	-0.498932638479098 (2.6)	a_4^{ψ} (r_4^{ψ})	0.256174912582562 (4.2)
B_2	8.6253238748137	a_5^{ϕ} (r_5^{ϕ})	-0.312337027098863 (2.8)	a_5^{ψ} (r_5^{ψ})	0.001524830500638 (5.0)
B_3	-2.186942690599	a_6^{ϕ} (r_6^{ϕ})	0.505803414854402 (3.0)	a^{ϕ}	-0.000046410598650
		a_7^{ϕ} (r_7^{ϕ})	2.594425601285000 (3.6)		
		a_8^{ϕ} (r_8^{ϕ})	-2.965136782893440 (3.8)		
		a_9^{ϕ} (r_9^{ϕ})	1.826825215082330 (4.2)		
		a_{10}^{ϕ} (r_{10}^{ϕ})	-1.465816770764790 (4.4)		
		a_{11}^{ϕ} (r_{11}^{ϕ})	1.069900083029370 (4.6)		
		a_{12}^{ϕ} (r_{12}^{ϕ})	-0.612976494212410 (4.8)		
		a_{13}^{ϕ} (r_{13}^{ϕ})	0.082454637432000 (5.2)		

of SIA and dislocation properties with this potential remains largely to be verified. At the moment, therefore, Mendeleev-type potentials appear to be the first choice in order to “extend DFT” to larger scales and this justifies their widespread use, also for the development of Fe alloy potentials [16–21]. Much can certainly be learnt by exploiting these potentials as they are.

Nonetheless, many limitations remain. In particular, it is difficult to decide about the reliability of these potentials when applied to cases for which there is no DFT reference, as experiments provide more qualitative, than quantitative, indications. The clearest example of this situation is given by SIA loops, which are, on the other hand, key to understanding and quantifying radiation damage evolution. In addition, even when a DFT reference does exist, the performance is not always satisfactory, as shown in the case of the non-parallel SIA cluster configurations or, to a lesser extent, in the case of dislocations. In spite of all efforts, a fully reliable description of SIA clusters and dislocations with interatomic potentials remains, therefore, an elusive objective that calls for further effort within the concerned scientific community.

Acknowledgements

This work was performed in the framework of the Perfect IP, partially funded by the European Commission, under contract FI60-CT-2003-508840. Thanks to G. Monnet for useful suggestions concerning the part on dislocations and to L. Ventelon for providing her data.

Appendix A

The M07 potential benchmarked in this article was developed following the same approach as for the M03 and A04 potentials. The same analytical form was used, namely with an embedding function including a term proportional to the square of the density in addition to the square root term characteristic of tight-binding potentials in the second moment approximation, such as Finnis–Sinclair potentials [90]. As in Ref. [1], the pairwise term and the density function are written as cubic splines, but the number of parameters was re-equilibrated between the two parts, by reducing from 15 to 13 the number of nodes in the pairwise term, and increasing it from 3 to 5 in the density function. The database used for the fit of the parameters was slightly modified. Concerning *ab initio* data, no data from liquid iron were used, instead more configurations were considered for the self-interstitial formation energies (i.e. including the tetrahedral and octahedral configurations) and the vacancy formation and migration energies were added. For the latter, we used the values obtained from DFT–GGA calculations carried out with the SIESTA code using 250 atom cells. As in Ref. [1], an exponential function ensures a smooth connexion with the Biersack–Ziegler repulsion at short distance. The *ab initio* values of the fcc lattice parameter as well as the fcc–bcc energy difference were also taken into account. Among the tests performed on the obtained potentials, a particular attention was paid to improve, with respect to M03 and A04, on the one hand, the thermal expansion and, on the other hand, the vacancy migration barrier, as compared to experiment / *ab initio* results.

We have adopted as fitting tool the ASSIMPOT code (T. Dagusé and G. Bencteux, unpublished), which is based on the principle of variational assimilation. The deviation between the results provided by a set of parameters and the target values of the fitting database is quantified using an objective function. This objective function is minimized using conjugate gradient technique. We tried to include the defect configurations, i.e. their relaxed *ab initio* atomic positions, in the database by including the forces, with a zero target value, in the objective function. In practice, it turns

out that it is impossible to fit energies and forces simultaneously: if one relaxes the positions with the obtained potential, relaxed energies deviate from their objective values. In other words, DFT–GGA and EAM force fields around defects differ significantly. This type of fitting is therefore used only in the first step. Then, the atomic positions are no longer considered in the fit and, for every defect, the energies are calculated using the atomic positions relaxed for the previous set of parameters. This procedure is iterated until convergence. Several converged sets of parameters were obtained using this methodology. The set of parameters selected for the present paper is given in Table 10.

References

- [1] M.I. Mendeleev, S. Han, D.J. Srolovitz, G.J. Ackland, D.Y. Sun, M. Asta, *Philos. Mag.* 83 (2003) 3977.
- [2] M.S. Daw, M.I. Baskes, *Phys. Rev. B* 29 (1984) 6443.
- [3] C. Domain, C.S. Becquart, *Phys. Rev. B* 65 (2001) 024103.
- [4] F. Willaime, C.C. Fu, M.C. Marinica, J. Dalla Torre, *Nucl. Instrum. Methods B* 192 (2005) 228.
- [5] C. Domain, G. Monnet, *Phys. Rev. Lett.* 95 (2005) 215506.
- [6] G.J. Ackland, M.I. Mendeleev, D.J. Srolovitz, S. Han, A.V. Barashev, *J. Phys.: Condens. Matter* 16 (2004) S2642.
- [7] D. Terentyev, C. Lagerstedt, P. Olsson, K. Nordlund, J. Wallenius, C.S. Becquart, L. Malerba, *J. Nucl. Mater.* 351 (2006) 65.
- [8] D. Terentyev, L. Malerba, M. Hou, *Phys. Rev. B* 75 (2007) 104018.
- [9] D. Terentyev, L. Malerba, D.J. Bacon, Yu.N. Osetsky, *J. Phys.: Condens. Matter* 19 (2007) 456211.
- [10] C. Björkas, K. Nordlund, *Nucl. Instrum. Methods Phys. Res. B* 259 (2007) 853–860.
- [11] M.-C. Marinica, F. Willaime, *Solid State Phenom.* 129 (2007) 67.
- [12] D. Terentyev, T.P.C. Klaver, P. Olsson, M.-C. Marinica, F. Willaime, C. Domain, L. Malerba, *Phys. Rev. Lett.* 100 (2008) 145503; For NPC see also: F. Gao, D.J. Bacon, Yu.N. Osetsky, P.E.J. Flewitt, T.A. Lewis, *J. Nucl. Mater.* 276 (2000) 213.
- [13] D. Terentyev, L. Malerba, *J. Nucl. Mater.* 377 (2008) 141.
- [14] D. Terentyev, L. Malerba, P. Klaver, P. Olsson, *J. Nucl. Mater.* 382 (2008) 126.
- [15] D. Terentyev, D.J. Bacon, Yu.N. Osetsky, *J. Phys.: Condens. Matter* 20 (2008) 445007.
- [16] A. Caro, D.A. Crowson, M. Caro, *Phys. Rev. Lett.* 95 (2005) 075702.
- [17] P. Olsson, J. Wallenius, C. Domain, K. Nordlund, L. Malerba, *Phys. Rev. B* 72 (2005) 214119.
- [18] R.C. Pasianot, L. Malerba, *J. Nucl. Mater.* 360 (2007) 118.
- [19] G. Bonny, R.C. Pasianot, L. Malerba, *Model. Simulat. Mater. Sci. Eng.* 17 (2009) 025010.
- [20] G. Bonny, R.C. Pasianot, N. Castin, L. Malerba, *Philos. Mag.* 89 (2009) 3531.
- [21] D.J. Hepburn, G.J. Ackland, *Phys. Rev. B* 78 (2008) 165115.
- [22] S. Dudarev, P.M. Derlet, *J. Phys.: Condens. Matter* 17 (2005) 7097 (case study II).
- [23] C.-C. Fu, F. Willaime, P. Ordejón, *Phys. Rev. Lett.* 92 (2004) 175503.
- [24] G.J. Ackland, D.J. Bacon, A.F. Calder, T. Harris, *Philos. Mag.* A 75 (1997) 713.
- [25] M. Pelfort, Yu.N. Osetsky, A. Serra, *Philos. Mag.* 81 (2001) 803.
- [26] J. Marian, B.D. Wirth, J.M. Perlado, G.R. Odette, T. Díaz de la Rubia, *Phys. Rev. B* 64 (2001) 094303.
- [27] J. Marian, B.D. Wirth, A. Caro, B. Sadigh, G.R. Odette, J.M. Perlado, T. Díaz de la Rubia, *Phys. Rev. B* 65 (2002) 144102.
- [28] J. Marian, B.D. Wirth, J.M. Perlado, *Phys. Rev. Lett.* 88 (2002) 255507.
- [29] M.A. Puigvi, Yu.N. Osetsky, A. Serra, *Philos. Mag.* 83 (2003) 857.
- [30] M.A. Puigvi, Yu.N. Osetsky, A. Serra, *Mater. Sci. Eng. A* 365 (2004) 101.
- [31] Yu.N. Osetsky, D.J. Bacon, *Model. Simulat. Mater. Sci. Eng.* 11 (2003) 427.
- [32] Yu.N. Osetsky, D.J. Bacon, *J. Nucl. Mater.* 323 (2003) 268.
- [33] Yu.N. Osetsky, D.J. Bacon, Z. Rong, B.N. Singh, *Philos. Mag. Lett.* 84 (2004) 745.
- [34] Z. Rong, V. Mohles, D.J. Bacon, Yu.N. Osetsky, *Philos. Mag.* 85 (2005) 171.
- [35] Z. Rong, Yu.N. Osetsky, D.J. Bacon, *Philos. Mag.* 85 (2005) 1473.
- [36] Z. Rong, D.J. Bacon, Yu.N. Osetsky, *Mater. Sci. Eng. A* 400–401 (2005) 378.
- [37] M. Müller, P. Erhart, K. Albe, *J. Phys.: Condens. Matter* 19 (2007) 326220.
- [38] G. Simmons, H. Wang, *Single Crystal Elastic Constants and Calculated Aggregate Properties: A Handbook*, MIT Press, Cambridge, 1971.
- [39] C. Kittel, *Introduction to Solid State Physics*, sixth ed., John Wiley and Sons, Inc., New York, Chichester, Brisbane, Toronto, Singapore, 1987.
- [40] E.G. Moroni, G. Kresse, J. Hafner, J. Furthmüller, *Phys. Rev. B* 56 (1997) 15629.
- [41] T. Kraft, M. Methfessel, M. van Schilfaarde, M. Scheffler, *Phys. Rev. B* 47 (1993) 9862.
- [42] W. Bendick, W. Pepperhof, *Acta Metall.* 30 (1982) 679.
- [43] J.A. Rayne, B.S. Chandrasekhar, *Phys. Rev. B* 122 (1961) 1714.
- [44] B.N. Brockhouse, H.E. Abou-Helal, E.D. Hallman, *Solid State Commun.* 5 (1967) 211.
- [45] C.J. Smithells, *Metals Reference Book*, Butterworths, London, 1967.
- [46] D.R. Lide (Ed.), *Handbook of Chemistry and Physics*, 85th ed., CRC Press, Boca Raton, FL, 2004.
- [47] P. Van Zwol, P.M. Derlet, H. Van Swygenhoven, S.L. Dudarev, *Surf. Sci.* 601 (16) (2007) 3512.

- [48] E. Lopasso, M. Caro, A. Caro, P.E.A. Turchi, Phys. Rev. B 68 (2003) 214205.
- [49] F. Ercolessi, A Molecular Dynamics Primer, Spring College in Computational Physics, ICTP, Trieste, June 1997. <<http://www.fisica.uniud.it/~ercolessi/md/>>.
- [50] G. Kresse, J. Hafner, Phys. Rev. B 47 (1993) 558;
G. Kresse, J. Hafner, Phys. Rev. B 49 (1994) 14251;
G. Kresse, J. Furthmüller, Phys. Rev. B 54 (1996) 11169;
G. Kresse, J. Furthmüller, Comput. Mater. Sci. 6 (1996) 15.
- [51] J.P. Perdew, K. Burke, M. Ernzerhof, Phys. Rev. Lett. 77 (1996) 3865.
- [52] P.E. Blöchl, Phys. Rev. B 50 (1994) 17953.
- [53] G. Kresse, D. Joubert, Phys. Rev. B 59 (1999) 1758.
- [54] D. Vanderbilt, Phys. Rev. B 41 (1990) 7892.
- [55] G. Kresse, J. Hafner, J. Phys.: Condens. Mater. 6 (1996) 8245.
- [56] J.P. Perdew, J.A. Chevary, S.H. Vosko, K.A. Jackson, M.R. Pederson, C. Fiolhais, Phys. Rev. B 46 (1992) 6671.
- [57] K. Nordlund, R.S. Averback, Phys. Rev. Lett. 80 (1998) 4201.
- [58] H.E. Schaefer, K. Maier, M. Weller, D. Herlach, A. Seeger, J. Diehl, Scripta Metall. 11 (1977) 803.
- [59] L.D. Schepper, D. Segers, L. Dorikens-Vanpraet, M. Dorikens, G. Knuyt, L.M. Stals, P. Moser, Phys. Rev. B 27 (1983) 5257.
- [60] P. Olsson, C. Domain, J. Wallenius, Phys. Rev. B 75 (2007) 014110.
- [61] P. Ehrhart, K.H. Robrock, H.R. Schober, in: R.A. Johnson, A.N. Orlov (Eds.), Physics of Radiation Effects in Crystals, Elsevier, Amsterdam, 1986, p. 63.
- [62] C.S. Becquart, C. Domain, Nucl. Instrum. Methods Phys. Res. B 202 (2003) 44.
- [63] C.-C. Fu, J. Dalla Torre, F. Willaime, J.-L. Bocquet, A. Barbu, Nature Mater. 4 (2005) 68.
- [64] F.G. Djurabekova, L. Malerba, C. Domain, C. Becquart, Nucl. Instrum. Methods Phys. Res. B 255 (2007) 47.
- [65] G. Henkelman, G. Jóhannesson, H. Jónsson, in: S.D. Schwartz (Ed.), Progress on Theoretical Chemistry and Physics, Kluwer Academic Publishers, 2000, p. 269.
- [66] G. Mills, H. Jónsson, Phys. Rev. Lett. 72 (1994) 1124;
G. Mills, H. Jónsson, G. Schenter, Surf. Sci. 324 (1995) 305.
- [67] F. Djurabekova, L. Malerba, R.C. Pasianot, P. Olsson, Philos. Mag. 90 (2010) 2585.
- [68] A. Vehanen, P. Hautojärvi, J. Johansson, J. Yli-Kaupilla, P. Moser, Phys. Rev. B 25 (1982) 762.
- [69] L.J. Cuddy, Acta Metall. 16 (1968) 23.
- [70] T. Tabata et al., Scripta Metall. 14 (1983) 1317.
- [71] H. Wollenberger, in: R. Cahn, P. Haasen (Eds.), Physical Metallurgy, vol. 2, North-Holland, 1996.
- [72] S.M.J. Gordon, S.D. Kenny, R. Smith, Phys. Rev. B 72 (2005) 214104.
- [73] V. Hivert, R. Pichon, H. Bilger, P. Bichon, J. Verdone, D. Dautreppe, P. Moser, J. Phys. Chem. Solids 31 (1970) 1843.
- [74] J. Verdone, W. Chambron, P. Moser, Phys. Status Solidi B 61 (1974) K41.
- [75] S. Takaki, J. Fuss, H. Kugler, U. Dedek, H. Schultz, Radiat. Eff. 79 (1983) 87.
- [76] F. Gao, G. Henkelman, W.J. Weber, L.R. Corrales, H. Jónsson, Nucl. Instrum. Methods Phys. Res. B 202 (2003) 1.
- [77] Yu.N. Osetsky, A. Serra, Defect Diffus. Forum 143–147 (1997) 155.
- [78] B.L. Eyre, A.F. Bartlett, Philos. Mag. 12 (1965) 261.
- [79] L. Malerba, G.J. Ackland, C.S. Becquart, G. Bonny, C. Domain, S. Dudarev, C.-C. Fu, D. Hepburn, M.C. Marinica, P. Olsson, R.C. Pasianot, J.M. Raulot, F. Soisson, D. Terentyev, E. Vincent, F. Willaime, Ab initio calculations and interatomic potentials for iron and iron alloys: achievements within the FP6/perfect project, J. Nucl. Mater. 406 (2010) 7.
- [80] V. Vitek, Cryst. Lattice Defects 5 (1974) 1.
- [81] F. Kroupa, Czech. J. Phys. B 10 (1960) 284.
- [82] S.L. Dudarev, R. Bullough, P.M. Derlet, Phys. Rev. Lett. 100 (2008) 135503.
- [83] K. Nordlund, J. Wallenius, L. Malerba, Nucl. Instrum. Methods Phys. Res. B 246 (2006) 322.
- [84] F. Maury, M. Biget, P. Vajda, A. Lucasson, P. Lucasson, Phys. Rev. B 14 (1976) 5303.
- [85] G. Wallner, M.S. Anand, L.R. Greenwood, M.A. Kirk, W. Mansel, W. Waschkowski, J. Nucl. Mater. 152 (1988) 146.
- [86] Annual Book of ASTM Standard E693-94, vol. 12.02, 1994.
- [87] C.H.M. Broeders, A.Yu. Konobeyev, J. Nucl. Mater. 328 (2004) 197.
- [88] C.S. Becquart, C. Domain, A. Legris, J.C. Van Duysen, J. Nucl. Mater. 280 (2000) 73.
- [89] L. Malerba, J. Nucl. Mater. 351 (2006) 28.
- [90] M.W. Finnis, J.E. Sinclair, Philos. Mag. A 50 (1984) 45.